



Auralization of vibroacoustic models in engineering using Wave Field Synthesis: Application to plates and transmission loss



A. Bolduc^{a,b}, P.-A. Gauthier^{a,b,*}, A. Berry^{a,b}

^a Groupe d'Acoustique de l'Université de Sherbrooke, Sherbrooke, Canada

^b Centre for Interdisciplinary Research in Music, Media, and Technology, Montréal, Canada

ARTICLE INFO

Article history:

Received 20 December 2016

Revised 15 August 2017

Accepted 16 August 2017

Available online 3 September 2017

Keywords:

Sound field reproduction

Wave Field Synthesis

Virtual acoustics

Extended sources

ABSTRACT

While perceptual evaluation and sound quality testing with jury are now recognized as essential parts of acoustical product development, they are rarely implemented with spatial sound field reproduction. Instead, monophonic, stereophonic or binaural presentations are used. This paper investigates the workability and interest of a method to use complete vibroacoustic engineering models for auralization based on 2.5D Wave Field Synthesis (WFS). This method is proposed in order that spatial characteristics such as directivity patterns and direction-of-arrival are part of the reproduced sound field while preserving the model complete formulation that coherently combines frequency and spatial responses. Modifications to the standard 2.5D WFS operators are proposed for extended primary sources, affecting the reference line definition and compensating for out-of-plane elementary primary sources. Reported simulations and experiments of reproductions of two physically-accurate vibroacoustic models of thin plates show that the proposed method allows for an effective reproduction in the horizontal plane: Spatial and frequency domains features are recreated. Application of the method to the sound rendering of a virtual transmission loss measurement setup shows the potential of the method for use in virtual acoustical prototyping for jury testing.

© 2017 Elsevier Ltd. All rights reserved.

1. Introduction

In acoustical engineering, vibroacoustic models are used to predict products acoustical responses. Results are traditionally evaluated with visual or numerical information, such as sound spectra, sound intensity fields or sound pressure levels. This is paradoxical since visual or numerical data is employed to provide information on, or convince potential customers of, sound-related phenomena. For instance, the Transmission Loss (TL) of aerospace panels is a common engineering measurement that is communicated by visual and numerical evaluation [1] (p. 137, Eq. (7.1)). However, a larger TL alone does not guarantee a better auditory perceptual comfort, but several product design decisions are still based on TL. The issue with purely visual or numerical representations of vibroacoustic models is that audible annoyances can be visually absent from such physical data representations. To circumvent this limitation of purely physical comparison metrics, perceptual evaluation and sound quality testing with jury are now recognized as an essential part of product development in several fields [2,3,4,5] (see for example [4], p. 1).

In this general and current context, auralization of theoretical acoustic models such as those found in architectural applications is now common [6–20]. However, for most auralization applications in architecture or sound quality of vehicles, the sound

* Corresponding author. Groupe d'Acoustique de l'Université de Sherbrooke, Sherbrooke, Canada.
E-mail address: philippe_aubert_gauthier@hotmail.com (P.-A. Gauthier).

is presented either as a monophonic, stereophonic or binaural mix. Only more recently [7,8] has auralization been investigated with clear emphasis on spatial sound reproduction using Near-Field-Compensated Higher-Order Ambisonics (NFC-HOA) [13,14] or Wave Field Synthesis (WFS) [15]. Also, in most of these cases of auralization of advanced acoustical models, applications were limited to architectural spaces [7]; or the idea has been proposed for vehicles, machines or architectural spaces yet without actual practical implementation (see [8], (p. 289–293)). Although there are more and more examples of auralization of architectures with spatial rendering, to the authors' knowledge, no systematic research has been conducted for the auralization of complex mechanical or vibratory models with spatial rendering using loudspeakers or WFS. As an example, no research of this type has been mentioned in a recent review on spatial sound and WFS [21]. This paper is an investigation in this emerging trend. Also, as pointed by Svensson [19], there are few publications on auralization (with or without spatial rendering) that include accuracy assessments, either based on listening tests or physical evaluations. Accordingly, this paper presents an exhaustive physical evaluation of the proposed method, through theoretical simulations and actual sound field measurements using a dedicated experimental setup. Therefore, although the motivation of this work lies in the idea of listening to physical models, the corresponding Sound Field Reproduction (SFR) must be physically evaluated in order to fulfill the expectations within an engineering and industrial application that requires physical validity.

Putting aside these rendering considerations, one notes that many vibroacoustic models used in engineering rely on advanced computing methods, such as analytical coupled models, Finite-Element-Method (FEM), Finite-Difference-Method or Boundary-Element-Method, that can predict sound fields in an extended spatial area. However, these powerful numerical simulation tools, developed and required in a mechanical or acoustical product design workflow, are rarely used to drive virtual auditory displays made of loudspeaker arrays, despite their great potential to act as refined, physically-valid, primary sound sources [22]. Following these observations, in this paper, we investigate the sound field reproduction of such vibroacoustic models as found in classical acoustical engineering contexts. Our primary aim is to include an extended primary source definition which includes both the spatial characteristics of sound radiation and the frequency responses based on vibration models where the classical model formulation of the modeled object is preserved.

With respect to current SFR technology and methods, WFS is generally used for SFR defined by a combination of plane or spherical waves, propagating in a horizontal listening plane. It is known that WFS can evoke accurate sound localization of the individual primary sound sources even when a multi-source sound field is synthesized [23], (p. 169). In Ref. [22], a brief review is made on techniques available to provide more refined WFS primary source definitions, such as how to give point sources a complex directivity pattern [24], or how to derive primary source signals and positions from real objects from physical modeling [25], physically-informed models [26], or from arbitrarily shaped sound sources [27].

Among these works [26,27] are the most closely related to this paper. In Ref. [26], the authors reproduce a sound field that could have been created by vibrating plates or spheres. To do so, they rely on primary monopole distribution that corresponds to a plate modal shape: a monopole is placed on each antinode of the modal shape. However, this cannot be considered as a complete sound field reproduction of vibroacoustic model for three reasons: 1) The authors do not take into account the frequency response of each mode. 2) Using primary monopoles only located according to a mode shape can only be physically representative of a plate for a very limited frequency band. Indeed the spatial radiation pattern is a complex interaction of mode shape, acoustical wavelength and plate size that often lead to radiation modes (edge modes, corner modes) that are different from the vibrational modes to describe the actual transversal displacement field of the vibrating plate [28]. This behavior cannot be recreated using the method proposed in Ref. [26]. 3) Only one mode shape is considered and exemplified in Ref. [26] and experimental evaluation is not provided. A full physically-valid plate model for SFR could only include a summation of vibrational modes [29], (p. 213–214). In [27], (Chap. 5), Baalman considers the SFR of more complex primary sources using triangulated meshes that wrap around extended primary sources. However, the actual dynamics of vibration of the primary source is not included.

In this paper, the general contribution is therefore to introduce an example of SFR of a fully integrated and consistent vibroacoustic model, i.e. the dynamic and spatial response of which that cannot be separated. To do so, this paper presents the illustrative case of a thin simply-supported plate. However, the proposed method is not limited to such analytical model.

The aforementioned works are used and were designed mainly for artistic purposes, or for physically-inspired, though still partial, mechanical modeling, and rely (in a way) on auditory perception cues to achieve reproduction of extended and complex objects. They do not represent the 3D sound field radiated by a physical object with specific structural and radiation behavior (such as resonance, dispersion, coincidence, radiation modes, surface modes, corner modes, edge modes, etc. [28], p. 67–76) defined by its geometry, boundary conditions and material properties. In this paper, an approach for WFS physical reproduction of vibroacoustic models is applied in a mechanical/acoustical engineering context. Here, we define a physical reproduction such that the reproduced sound field is only defined through, and must match, the target sound field radiated by the object. The proposed general method can be used to reproduce the sound fields of complex engineering models solved with analytical or numerical methods.

Since traditional 2.5D WFS operators [24] contain several simplifications that can not be circumvented by the problem definition used in this paper, modified 2.5D WFS operators are also proposed. The operators can process exterior and focused primary sources, in and out of the reproduction plane.

To sum-up, the contribution of this paper lies in the exploration of an extended primary source defined as physically-accurate vibroacoustic model where both spatial and frequency response are taken into account. This opens many research questions related to extended primary source and out-of-plane primary sources. Furthermore, starting with a simple case, this preliminary investigation of the thin plate paves the way to more complex applications and vibroacoustic models WFS rendering that can

be useful for sound quality studies and virtual acoustics in acoustical engineering.

The problem is defined in Section 2. In Section 3, the WFS of extended primary source is described. Section 4 discusses traditional 2.5D WFS operators limitations and proposed improvements to circumvent the specific challenges of extended primary source models. The studied cases are described in Section 5 in order to define the target sound field for the reported cases. The experimental setup is described in Section 6. Simulation and experimental results are reported in Section 7. In Section 8, the method is applied in an engineering context, by spatially rendering the sound field transmission problem.

2. Problem definition

The problem is illustrated in Fig. 1. An extended primary source (a plate for the cases reported herein) is positioned relative to a Secondary Source Distribution (SSD, the loudspeaker array). The center of the square SSD is the origin of the coordinate system. The extended primary source surface is discretized as a grid of elementary primary point sources with positions $\mathbf{x}_s = (x_s, y_s, z_s)$ (m) on the vibrating surface A_s . The extended primary source shows a transverse vibration velocity field $u_s(\mathbf{x}_s, \omega)$ (m/s) pulsating at ω (rad/s) along the normal \mathbf{n}_s . Note that subscript s indicates a reference to primary sources. The model is developed using continuous analytical equations and is discretized later on when numerical simulations and experiments are achieved.

Each secondary source has a position vector $\mathbf{x}_0 = (x_0, y_0, z_0)$ (m), is at Δx_0 from its neighbor, is located on a horizontal reproduction plane and points inward; the source velocity direction being relative to the normal vector \mathbf{n}_0 , representing the main axis of the loudspeaker when experiments are conducted. Note that subscript 0 generally indicates a reference to secondary sources. The problem is herein defined as how one should drive the reproduction loudspeakers to recreate the sound field produced by the extended primary source.

In this paper, the time convention for complex frequency-domain quantities is $e^{j\omega t}$.

3. WFS of extended primary source

3.1. Sound radiation of an extended primary source

The radiated sound field $P(\mathbf{x}, \omega)$ (Pa) of a baffled vibrating surface can be computed with the Rayleigh first integral:

$$P(\mathbf{x}, \omega) = \int_{A_s} G(\mathbf{x}, \mathbf{x}_s, \omega) j\omega \rho_0 u_s(\mathbf{x}_s, \omega) dA_s, \quad (1)$$

where $u_s(\mathbf{x}_s, \omega)$ is the transverse displacement field of the vibrating surface along \mathbf{n}_s , ρ_0 (kg/m^3) is the air density and $G(\mathbf{x}, \mathbf{x}_s, \omega)$ is the Green function verifying the Helmholtz equation of a baffled monopole in a free half-space [30]:

$$G(\mathbf{x}, \mathbf{x}_s, \omega) = \frac{e^{-jk\|\mathbf{x}-\mathbf{x}_s\|}}{2\pi\|\mathbf{x}-\mathbf{x}_s\|}, \quad (2)$$

with the acoustic wavenumber $k = \omega/c_0$ (rad/m), sound speed in air c_0 (m/s) and where $\|\cdot\|$ denotes the Euclidean norm. Depending on the modeling method, P can also be computed numerically. In this paper, a discretized radiation model is used so that the method can be implemented for FEM models of the structural response, where u_s is often provided for a surface mesh. P is therefore the target sound field that should be reproduced.

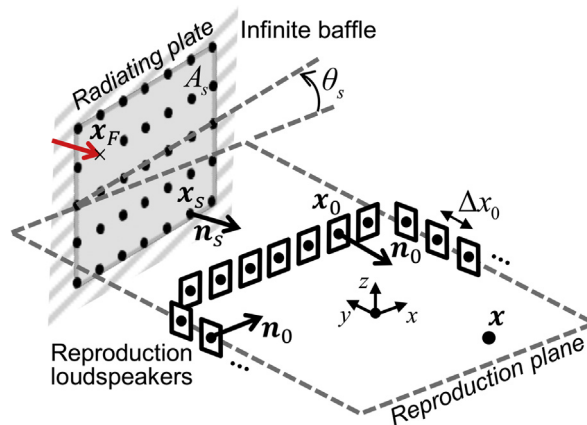


Fig. 1. Geometric parameters of the problem definition exemplified for a radiating plate in an infinite baffle: \mathbf{x} is an observation point; \mathbf{x}_0 is the location of a reproduction source; \mathbf{n}_0 is a unit vector along the principal axis of the reproduction source in \mathbf{x}_0 ; \mathbf{x}_s is the location of an elementary primary source; \mathbf{n}_s is a unit vector normal to A_s in \mathbf{x}_s ; \mathbf{x}_F is the point of force excitation on the radiating plate. The origin of the coordinate system is at the center of the square SSD.

3.2. 3D WFS driving function for an extended primary source

For 3D WFS, using an areal SSD, the Rayleigh first integral is evaluated for an area (for example, a planar SSD) to compute the reproduced sound field S_{3D} (Pa):

$$S_{3D}(\mathbf{x}, \omega) = - \int_{A_0} G(\mathbf{x}, \mathbf{x}_0, \omega) D_{3D}(\mathbf{x}_0, \omega) d\mathbf{x}_0 dz_0, \quad (3)$$

where A_0 is the SSD and the secondary source driving function D_{3D} is given by:

$$D_{3D}(\mathbf{x}_0, \omega) = -j\omega\rho_0 u_0(\mathbf{x}_0, \omega). \quad (4)$$

To find u_0 (m/s), the air particle velocity along \mathbf{n}_0 , at each secondary source location \mathbf{x}_0 , Eq. (1) can be combined to the Euler equation

$$j\omega\rho_0 \mathbf{u}_0(\mathbf{x}_0, \omega) = -\nabla P(\mathbf{x}_0, \omega), \quad (5)$$

where \mathbf{u}_0 (m/s) is the air particle velocity vector of the target sound field P at each secondary source location \mathbf{x}_0 . Then, from the Rayleigh integral Eq. (1) and the geometric definitions shown in Fig. 2, one finds:

$$u_0(\mathbf{x}_0, \omega) = - \int_{A_s} \frac{\partial G(\mathbf{x}_0, \mathbf{x}_s, \omega)}{\partial r_0} \frac{\partial r_0}{\partial n_0} u_s dA_s, \quad (6)$$

where $\partial/\partial n_0$ notation indicates partial derivative with respect to the normal vector \mathbf{n}_0 and where $r_0 = \|\mathbf{r}_0\|$. Also:

$$\frac{\partial G(\mathbf{x}_0, \mathbf{x}_s, \omega)}{\partial r_0} = -\frac{e^{-jk r_0}}{2\pi r_0} \left(\frac{1}{r_0} + jk \right) \quad (7)$$

and

$$\frac{\partial r_0}{\partial n_0} = \cos(\phi)\cos(\beta), \quad (8)$$

u_0 is then given by

$$u_0 = - \int_{A_s} \frac{\zeta e^{\zeta jk r_0}}{2\pi r_0} \left(\frac{1}{r_0} - \zeta jk \right) \cos(\phi)\cos(\beta) u_s dA_s, \quad (9)$$

where ϕ , β and \mathbf{r}_0 are illustrated in Fig. 2 with $\mathbf{r}_0 = \mathbf{x}_0 - \mathbf{x}_s$. For the development of the WFS operators, we define $\zeta = -1$ for exterior primary sources and $\zeta = 1$ for focused primary sources. In the next section, the 2.5D implementation and stationary phase point approximation is discussed in the specific case of an extended primary source.

4. 2.5D WFS of an extended primary source

As mentioned earlier, the approach relies on classical WFS formulation and formalism. However, there is a need for specific 2.5D WFS operators for physical SFR of spatially-extended primary sources. It is reminded that the 2.5D simply refers to an approximation of 3D WFS using a linear array of secondary sources. In this paper, the proposed 2.5D WFS operators are exemplified for an enclosing square SSD, but they remain transposable to any arbitrarily-shaped array composed of multiple linear distributions and not necessarily enclosing a listening area. A further requirement is that the modified operators must be compatible with exterior and focused primary sources, lying in or out of the reproduction plane.

Consequently, the following adaptations are proposed and described in the next sections:

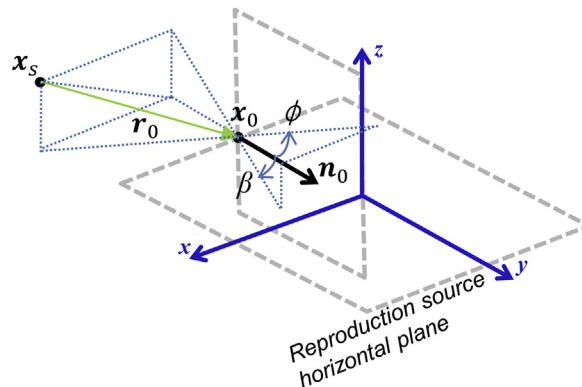


Fig. 2. Definition of β , ϕ and \mathbf{r}_0 for 3D WFS.

1. An elementary-primary-source-dependent reference line is defined (Section 4.1).
2. For each elementary primary source in $\mathbf{x}_s \in A_s$ and for each reproduction source in \mathbf{x}_0 with $z_0 = 0$, a virtual reproduction source is identified and located at the stationary phase point (above or below \mathbf{x}_0) for this specific pair of sources (Section 4.2).
3. An elementary contribution of this virtual reproduction source is computed based on the propagation distance from the elementary primary source in \mathbf{x}_s to the position of the virtual reproduction source (Section 4.2).
4. This elementary contribution to the virtual reproduction source is compensated:
 - (a) For the stationary phase approximation (Section 4.3).
 - (b) In gain and phase for its virtual location with respect to the actual reproduction source that will receive the final driving signals (Section 4.4).
 - (c) Based on active secondary selection and tapering (Section 4.5)
5. The driving signal for a reproduction source in \mathbf{x}_0 with $z_0 = 0$ is therefore obtained from the combination of all virtual reproduction sources above and below \mathbf{x}_0 .

4.1. Elementary-primary-source-dependent reference line

The selection of a reference line appears in the Stationary Phase Approximation (SPA) of the 2.5D WFS operator. The reference line is a selected line where the SPA error should be null. When dealing with a piecewise linear SSD, an intuitive approach for the definition of the reference lines is to rely on lines parallel to each linear segments of the reproduction loudspeaker array. These reference lines would be used for all exterior and focused primary sources. However, in this case, a focused extended primary source may intersect with one of the reference lines, thus resulting in amplitude and phase errors in the listening area, or instability in the WFS operators. To circumvent this problem, a different reference line positioning is introduced in this paper.

For each elementary primary source position \mathbf{x}_s , an associated elementary-primary-source-dependent reference line is defined in the horizontal plane as a line coincident with the center of the SSD and perpendicular to the elementary primary source position vector \mathbf{x}_s projected on the reproduction plane, as shown in Fig. 3. Since the distance between a linear SSD and a reference line is no longer the same for all secondary sources, three geometric variables need to be introduced to achieve the SPA in the derivation of the 2.5D WFS operator. These variables are shown in Fig. 3 γ is the distance, in the horizontal plane, between the elementary primary source \mathbf{x}_s and the point on its reference line \mathbf{x} along a line passing through the secondary source in \mathbf{x}_0 . α is the point-to-line distance between the secondary source \mathbf{x}_0 and a reference line for a given elementary primary source. Finally, ψ is the angle between two lines in the horizontal plane: 1) the line that passes by the center of the SSD and by \mathbf{x}_s 2) the line between \mathbf{x}_s and the source position \mathbf{x}_0 . These variables are obtained as follows:

$$\gamma = \frac{\|\mathbf{x}_s\|}{|\cos \psi|} \Big|_{z_s=0} \quad (10)$$

$$\psi = \arctan \frac{\|\mathbf{x}_s / \|\mathbf{x}_s\| \times (\mathbf{x}_0 - \mathbf{x}_s)\|}{\mathbf{x}_s / \|\mathbf{x}_s\| \cdot (\mathbf{x}_0 - \mathbf{x}_s)} \Big|_{z_s=0} = \arctan \frac{\|\mathbf{x}_s \times (\mathbf{x}_0 - \mathbf{x}_s)\|}{\mathbf{x}_s \cdot (\mathbf{x}_0 - \mathbf{x}_s)} \Big|_{z_s=0} \quad (11)$$

$$\alpha = \mathbf{x}_0 \cdot \frac{\mathbf{x}_s}{\|\mathbf{x}_s\|} \Big|_{z_s=0} \quad (12)$$

where ψ was found using the cross and dot products fraction to obtain a ratio of sine and cosine terms. With these definitions, negative values of α occur for half the number of secondary sources, but their driving functions will be nullified later by the selection criterion, as detailed in Section 4.5. These three geometric variables are used below in the definition of the compensation factors and for the active reproductions source selection. Equations (10) and (11) are used in the SPA reported in Appendix. The correction factors will depend on α as introduced in Eq. (12).

4.2. Stationary phase approximation and stationary phase point

The 3D WFS implementation of Eqs. (3) and (4) suggests a need for reproduction sources along \mathbf{x}_0 and z_0 . This involves too many reproduction sources for practical implementation. To this end, 2.5D WFS was introduced [23] to avoid the need for reproduction sources along z_0 . To do so, the SPA is used for the integration along z_0 . In this case, the reproduced sound field and driving functions are given by the Rayleigh first integral combined with the tapering and secondary source selection window W , the dimensional factor Q_d and the out-of-plane primary sources compensation factor Q_c which are detailed in the next section. Note that these factors are functions of the elementary primary source \mathbf{x}_s and secondary source position \mathbf{x}_0 . Thus the 2.5D driving function $D(\mathbf{x}_0, \omega)$ is a modified version of the 3D driving function of Eqs. (3), (4) and (9) so that the reproduced sound field is given by:

$$S(\mathbf{x}, \omega) = - \int_{A_0} G(\mathbf{x}, \mathbf{x}_0, \omega) D(\mathbf{x}_0, \omega) d\mathbf{x}_0. \quad (13)$$

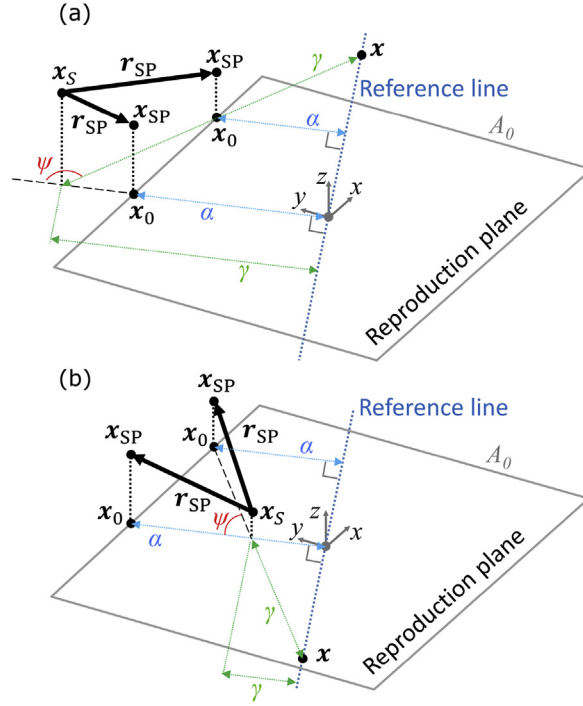


Fig. 3. Geometric variables γ , ψ and α , illustrated for one elementary primary source in \mathbf{x}_s and two secondary sources in \mathbf{x}_0 , for exterior (a) or focused (b) primary sources. The gray square represents the SSD.

where A_0 is now a linear SSD. This driving function D is now derived for a reproduction source in \mathbf{x}_0 based on u_0 not in \mathbf{x}_0 but at the stationary phase points $\mathbf{x}_{SP}(\mathbf{x}_0, \mathbf{x}_s)$ (the definition of \mathbf{x}_{SP} is further discussed below):

$$D(\mathbf{x}_0, \omega) = -j\omega\rho_0 u_0(\mathbf{x}_{SP}, \omega), \quad (14)$$

For the 2.5D case, u_0 is now given by the integration over the extended primary source of the source vibrational field u_s , as for the 3D case provided in Eq. (9), with the aforementioned correction factors:

$$u_0(\mathbf{x}_0, \omega) = - \int_{A_s} \frac{\zeta e^{\zeta j k r_{SP}}}{2\pi r_{SP}} \left(\frac{1}{r_{SP}} - \zeta j k \right) \cos(\phi) Q_c(\mathbf{x}_0, \mathbf{x}_s) Q_d(\mathbf{x}_0, \mathbf{x}_s) W(\mathbf{x}_0, \mathbf{x}_s) u_s dA_s. \quad (15)$$

It should be noted that in latter equation, the $\cos(\beta)$ term as found in Eq. (9) is removed. This $\cos(\beta)$ corrects for the angle propagation with respect to the reproduction plane for elementary primary sources outside the reproduction plane. However, in the forthcoming, the compensation for elementary sources outside the reproduction plane will be implemented by Q_c . Therefore, $\cos(\beta)$ is not included in Eq. (15).

Since a linear SSD is used and since a compensation for out-of-plane elementary primary sources is required, u_0 is therefore computed at $\mathbf{x}_{SP}(\mathbf{x}_s, \mathbf{x}_0) = (x_0, y_0, z_{SP})$ (m) (instead of \mathbf{x}_0 as in Eq. (3)). In Eq. (15), the propagation is therefore based on the distance between \mathbf{x}_s and \mathbf{x}_{SP} (also shown in Fig. 3) for the derivation of u_0 that appears in the driving function Eq. (14):

$$r_{SP} = \|\mathbf{r}_{SP}\| = \|\mathbf{x}_{SP} - \mathbf{x}_s\| \quad (16)$$

The vector \mathbf{x}_{SP} is the stationary phase point along z_s , introduced in the SPA method [31] to derive 2.5D WFS operators in Section 4.4 (see also Appendix). One can find \mathbf{x}_{SP} geometrically for each combination of elementary primary source \mathbf{x}_s and secondary source \mathbf{x}_0 by tracing a line between \mathbf{x}_s and \mathbf{x} (that belongs to the reference line) that passes over $\mathbf{x}_0 = (x_0, y_0, 0)$. This gives x_0, y_0 and z_{SP} as shown in Fig. 4 for both cases of exterior or focused primary sources. Typically, the stationary phase point \mathbf{x}_{SP} is given for $\mathbf{x}_0, \mathbf{x}_s$ as the closest point in z_{SP} from \mathbf{x}_s along a vertical line in \mathbf{x}_0 . Since the two triangles linking $\mathbf{x}, \mathbf{x}_{SP}, \mathbf{x}_0$ and $\mathbf{x}, \mathbf{x}_s, \mathbf{x}_s|_{z_s=0}$, respectively, are similar triangles, z_{SP} is directly obtained geometrically. Therefore, for elementary primary sources in the reproduction plane, $z_{SP} = 0$ and for any elementary source position, the stationary phase point is:

$$z_{SP}(\mathbf{x}_0, \mathbf{x}_s) = z_s \frac{\gamma + \zeta \|\mathbf{x}_0 - \mathbf{x}_s\|_{z_s=0}}{\gamma} \quad (17)$$

where γ depends on the reference line definition. Selection of the reference line is introduced in the next section. Note that \mathbf{x} belongs to the reference line where the SPA error should be null.

To sum up, for the proposed 2.5D implementation of extended primary source, the driving function is computed based on a virtual reproduction source in \mathbf{x}_{SP} but driving a real reproduction source in \mathbf{x}_0 . The compensation factors Q_c and Q_d are introduced in Sections. 4.3, 4.4 and 4.5 to compensate such approximations.

4.3. Correction factor Q_d

In this paper, since the Rayleigh first integral is used on a line instead of an area to compute a 2.5D WFS driving function, the SPA involves a dimensional factor Q_d (m) in Eq. (15). As discussed for single primary source in previous work [22], the classical correction factor $Q_t = \sqrt{2\pi y_{\text{ref}}/jk}$ [24], with constant distance y_{ref} (m) between the linear SSD and its parallel reference line, is not physically exact when the primary wave to be reproduced is different from a plane wave propagating in a direction perpendicular to a linear SSD. Knowing the angle θ_{PW} between the linear SSD and the plane wavefront direction, a simple proposed correction was $Q_{\text{PW}} = \sqrt{2\pi y_{\text{ref}} \sin \theta_{\text{PW}}/jk}$ [32]. When a primary source is represented by a point source instead of a plane wave, the $kr_0 \gg 1$ hypothesis states that the spherical wavefront is flat enough when crossing the SSD, such that it is considered as a plane wave. This means that, in order to use Q_{PW} , the primary source must be at a certain distance from the array.

In this paper, exterior and focused elementary primary point sources can be in close proximity of the SSD, so that the wavefronts are not sufficiently planar while crossing the SSD. Therefore, the aforementioned Q_{PW} that relies on the aforementioned hypothesis cannot be used. This is expressed by the condition $kr_0 \not\gg 1$. In classical 2.5D WFS, the $kr_0 \gg 1$ hypothesis is applied, so that the term $1/r_0$ in Eq. (9) tends to 0 and vanishes in comparison with jk . Since this work uses the $kr_0 \not\gg 1$ hypothesis, $\partial G/\partial r_0$ is kept intact in Eq. (6). In response to the problems discussed in this subsection, a different dimensional factor Q_d , defined for exterior and focused primary sources, is therefore used in this paper. It combines terms derived in the SPA when $kr_0 \not\gg 1$:

$$Q_d(\mathbf{x}_0, \mathbf{x}_s) = \sqrt{-\zeta} \sqrt{\frac{\zeta j 2\pi}{k}} \sqrt{\frac{-\zeta \alpha r_{\text{SP}}}{\alpha + \|\mathbf{x}_0 - \mathbf{x}_s\| \Big|_{z_s=0}}} \quad (18)$$

The first right-hand side term $\sqrt{-\zeta}$ accounts for the frequency independent phase shift of -90° when focused primary sources are reproduced, such as in [24], [Appendix A]. The second term $\sqrt{\zeta j 2\pi/k}$ comes from a part of the SPA formula [31] (see Appendix, Eq. (39)). The third term comes from the geometric choice of the reference line to remove the \mathbf{x} dependency from the result of the SPA [33], [Appendix C]. Since the reference line is not parallel to the linear SSD, it needs to be written in another form than the classical form [24], [Section 2.3].

4.4. Correction factor Q_c for out-of-plane elementary primary sources

Baalman [34] introduced a compensation factor for the reproduction of primary sources out of the reproduction plane, when using a linear SSD, so that there is no delay or amplitude error for a listener on the reference line. Baalman combined this compensation factor with the classical 2.5D WFS operator for a linear SSD, based on the Rayleigh first integral, the $kr_0 \gg 1$ hypothesis and the SPA method with the compensation factor Q_t discussed in Section 4.3 [24]. This factor can only be used if the reference line is parallel to the linear SSD and so does not apply to the problem as defined in this paper. This is due to the fact that the elevation of the stationary phase point z_{SP} is different for each secondary source and elementary primary source combination, as shown in Fig. 4.

For out-of-plane elementary primary sources, the associated driving functions are computed for a virtual out-of-plane secondary source located in \mathbf{x}_{SP} (Fig. 4) as in Eq. (15), so that the reproduced sound field S matches P on the reference line, instead of the actual secondary sources used for the physical reproduction. Since all time-domain driving functions from each out-of-plane and in-plane primary sources are summed at each secondary source, and since this summed signal is reproduced by an in-plane only secondary source, the out-of-plane content of the summed driving signal would be louder and in advance at the reference line, because $\|\mathbf{x}_0 - \mathbf{x}\| \leq \|\mathbf{x}_{\text{SP}} - \mathbf{x}\|$. Therefore, a factor Q_c combining an amplitude and a delay compensation is defined to realign the out-of-plane driving functions so that they arrive with proper delays and amplitudes for a listener on the reference line. It is given by a gain reduction:

$$g_c(\mathbf{x}_0, \mathbf{x}_s) = \frac{\alpha}{\sqrt{z_{\text{SP}}^2 + \alpha^2}} \quad (19)$$

and propagation time compensation:

$$\beta_c(\mathbf{x}_0, \mathbf{x}_s) = -k \left(\sqrt{z_{\text{SP}}^2 + \alpha^2} - \alpha \right) \quad (20)$$

so that:

$$Q_c(\mathbf{x}_0, \mathbf{x}_s) = g_c e^{j\beta_c} = \frac{\alpha}{\sqrt{z_{\text{SP}}^2 + \alpha^2}} e^{-jk \left(\sqrt{z_{\text{SP}}^2 + \alpha^2} - \alpha \right)} \quad (21)$$

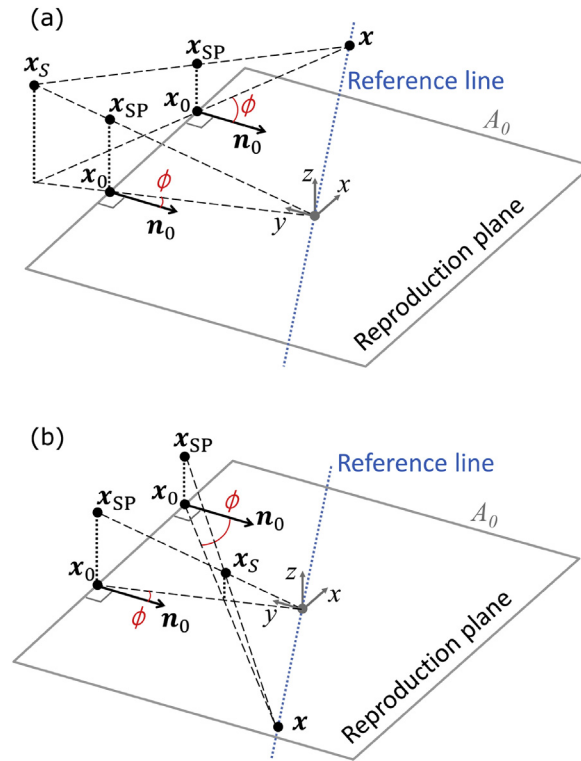


Fig. 4. Geometric construction of angle ϕ and stationary phase point \mathbf{x}_{SP} , for one elementary primary source in \mathbf{x}_s and two secondary sources in \mathbf{x}_0 , for exterior (a) or focused (b) elementary primary sources. The gray square represents the SSD.

4.5. Active secondary source selection and tapering

Because spatial discretization is used to imitate a continuous extended primary source, all the elementary primary sources in the spatial distribution representing the extended primary source will act together to imitate the extended primary source. Because of this spatial extent, the secondary source selection criterion and tapering window must be adapted to the specificity of the problem at hand. The proposed selection criterion and tapering strategy are shown in Fig. 5 and discussed in the following subsections.

4.5.1. Exterior elementary primary source

For each exterior elementary primary sources, the classical “illuminated” secondary sources method is used [32]. The secondary source selection criterion is straightforwardly defined for each elementary primary source as a rectangular window W_{rect}

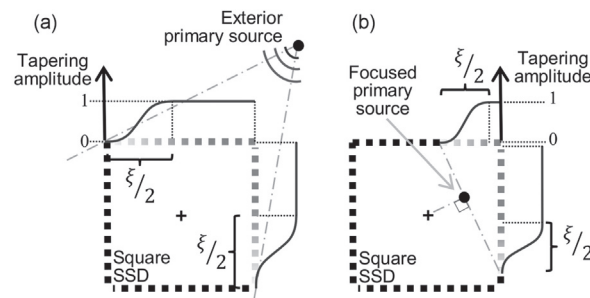


Fig. 5. Secondary source selection criteria (construction lines in gray - - -) and tapering windows (black continuous line —) for exterior (a) and focused (b) elementary primary sources. Black filled squares are the inactive secondary sources. The cross marker is the center of the SSD.

applied to the illuminated secondary sources:

$$W_{\text{rect}}(\mathbf{x}_0, \mathbf{x}_s) = \begin{cases} 1 & \text{if } \mathbf{u}_0(\mathbf{x}_s) \cdot \mathbf{n}_0(\mathbf{x}_0) > 0 \\ 0 & \text{if } \mathbf{u}_0(\mathbf{x}_s) \cdot \mathbf{n}_0(\mathbf{x}_0) \leq 0 \end{cases} \quad (22)$$

4.5.2. Focused elementary primary source

For an effective SFR over an extended listening area, a larger selection of active secondary sources is generally desired. This is successfully achieved with the illuminated secondary sources method for exterior sources. For extended focused sources, the active source criterion is not so intuitive, because the portion of the listening area where a converging sound field exists will increase with the number of active secondary sources. Thus, the effective listening area where the diverging reproduced sound field that matches the target sound field is free from a potentially destructive converging field will decrease, which is something that one should avoid.

To restrain, from the view point of a listener located in the center of the SSD, the converging part of the reproduced sound field behind the primary source, a secondary source selection criterion is defined for each focused elementary primary source. A line coincident with the elementary primary source position \mathbf{x}_s and perpendicular to the position vector \mathbf{x}_s is constructed (see right of Fig. 5). A rectangular window W_{rect} is applied between the two points where this line crosses the SSD and behind the elementary primary source. This is repeated for each elementary primary sources.

4.5.3. Spatial tapering

To reduce reproduction artifacts introduced by the spatial truncation of the SSD, a tapering window is applied to the active secondary sources [24,35] (see [24], [Section 2.4]). L_{on} is defined as the number of secondary sources matching the selection criterion, when the SSD is discretized.

A Tukey (cosine-shaped shoulders) window $W_{\text{Tukey}}(\mathbf{x}_0, \mathbf{x}_s)$ of length $L_{\text{on}} + 2$ with $\xi = 0.40$ is designed. The parameter ξ is the ratio of the cosine-tapered section length to the entire Tukey window length, with $0 \leq \xi \leq 1$. $L_{\text{on}} + 2$ is necessary to design a window of length L_{on} with no secondary source with a null weight on the extremities of the tapering window. The tapering value for the extremes of the window is denoted W_{floor} . W_{Tukey} is aligned with the non-null part of W_{rect} and is zero-padded to match the full length of W_{rect} .

The use of spatial tapering results in a reduction of the magnitude of the reproduction source inputs. Here, a compensation for this effect is introduced. When a physical reproduction is necessary, like in an engineering context, the total energy must be conserved by the WFS operators and the signal processing chain. Accordingly, at the reproduction stage, a manual gain can be used to fit the driving signals into the WFS system limits. Knowing that only one and unique gain is applied to all driving signals, it is easier to proceed with physical evaluation and take it in account.

In order to conserve the energy when a tapering window is applied to the SSD, a classical method borrowed from frequency domain signal processing is used. The correction factor depends on the window shape. In this paper, an energy conservation factor W_{EF} , depending on L_{on} for each elementary primary source, is computed for a Tukey window. The resulting window function $W(\mathbf{x}_0, \mathbf{x}_s)$ that is used as spatial tapering and as a selection criterion is:

$$W(\mathbf{x}_0, \mathbf{x}_s) = W_{\text{EF}} W_{\text{Tukey}} \quad (23)$$

with

$$W_{\text{EF}} = W_{\text{floor}} + (1 - W_{\text{floor}}) \left(\xi \sqrt{\frac{8}{3}} + (1 - \xi) \right) \quad (24)$$

5. Studied cases

5.1. Thin plate transverse vibration

In order to exemplify the proposed method, a classical analytical vibroacoustic model of a simply supported baffled thin plate is used to compute $u_s(\mathbf{x}_s, \omega)$. Details of the mode shapes and resonant frequency responses can be found in classical textbooks [29], (p. 213–214). In this paper, a vertical plate with an orientation θ_s ($^\circ$) in the x - y plane and with width a (m), height b (m) and thickness d (m) is used for the simulations and experiments. The case of forced vibration with a force $F(\omega)$ located in \mathbf{x}_f is studied in this paper. The case of simply-supported plate on all its boundaries is considered and x_a and z_a are the horizontal and vertical local coordinates on the plate surface with the plate centroid \mathbf{x}_c as the origin. In the plate response, one term is responsible for the frequency-dependent dynamical behavior of the model and the mode shapes are responsible for the spatial pattern of each eigenfunctions, each of which leads to a different directivity pattern as a function of frequency. To be qualified as an extended primary source, the plate dimensions need to be significant in comparison with the range of considered wavelengths. Indeed, for sources smaller than the wavelength, the sources can typically be replaced by single point sources that emit spherical waves. Note that the specificity of the selected model does not limit the scope of the proposed method. Indeed, the vibration velocity field u_s could have been obtained from any other type of model, such as FEM. In this paper, the plate was selected as an

Table 1

Geometric parameters of studied cases. The plate centroid position is given by \mathbf{x}_c . The point force position is $\mathbf{x}_F = (x_F \ 0 \ 0)$, given in the plate local coordinate system.

	a (m)	b (m)	d (m)	θ_s ($^\circ$)	\mathbf{x}_c (m)	x_F (m)	L_s	H_s
Ext.	6	4	0.015	180	(0 4 0)	-1	151	101
Foc.	1.2	0.8	0.003	200	(-0.5 1 0)	-0.2	61	41

illustrative test case.

In this paper, a vertical aluminum plate (Young’s modulus $E_s = 70$ GPa, density $\rho_s = 2700$ kg/m³, structural loss factor $\eta = 0.004$ and Poisson’s ratio $\nu = 0.33$) with an orientation θ_s ($^\circ$) in the x - y plane and with width a (m), height b (m) and thickness d (m) is used for the simulations and experiments. The air density value is $\rho_0 = 1.2041$ kg/m³ and sound speed in air is set to $c_0 = 343$ m/s.

Two cases of extended primary sources are studied: Exterior and focused plates. The parameters for these cases are shown in Table 1. Positions of the plates with respect to the SSD are shown in Fig. 6(c) and (d).

5.2. Spatial discretization and aliasing

When the discretization of A_s (i.e. the vibrating surface that acts as the extended primary source) is achieved, L_s and H_s specify the number of elementary primary source positions in the spatial grid along the width and height, respectively. The grid spacing is given by Δx_s (horizontally) and Δz_s (vertically) in the plate coordinate system. These discretization parameters are chosen in order to ensure that there is no spatial aliasing in the primary vibrating surface and resulting acoustic responses due to a discrete grid. The vibrating surface A_s is of dimension a by b . Accordingly, these criteria are used:

$$\max(\Delta x_s, \Delta z_s) = \frac{c_0}{2(f_s/2)} \tag{25}$$

$$\Delta x_s \leq a/(\max(m) + 1) \tag{26}$$

$$\Delta z_s \leq b/(\max(n) + 1) \tag{27}$$

with $f_s/2$ (Hz) the maximum frequency at which the vibroacoustic model frequency response is computed. f_s is the sampling frequency for the time-domain representation of the model. In these equations, $\max(n)$ and $\max(m)$ indicate the largest modal indexes n and m used in the plate model.

6. Experimental setup

The WFS loudspeaker array is a square, with each side having 24 loudspeakers and measuring 4 m, and with an inter-loudspeaker distance Δx_0 of 0.165 m. The spatial-aliasing-free frequency range of each side is below 1040 Hz, due to the inter-loudspeaker distance [32]. The square array is approximately centered in a $6.1 \times 5.7 \times 3.3$ m room with concrete walls or

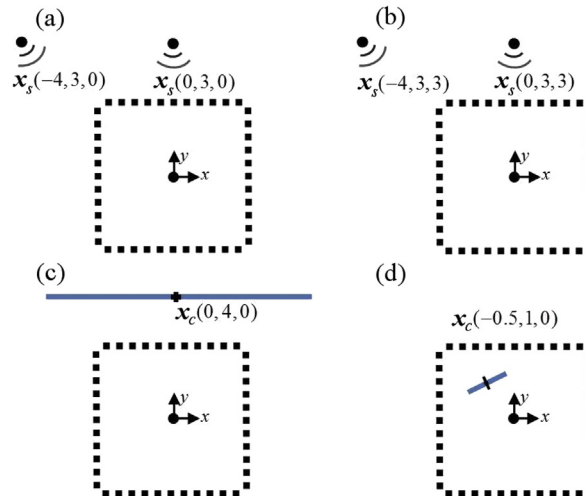


Fig. 6. Positions of the single and extended primary sources. (a) and (b): Validation cases with two in-plane and out-of-plane, respectively, primary sources. (c): Exterior plate shown as thick line. (d): Focused plate shown as thick line. The SSD is schematically shown as thick dotted lines.

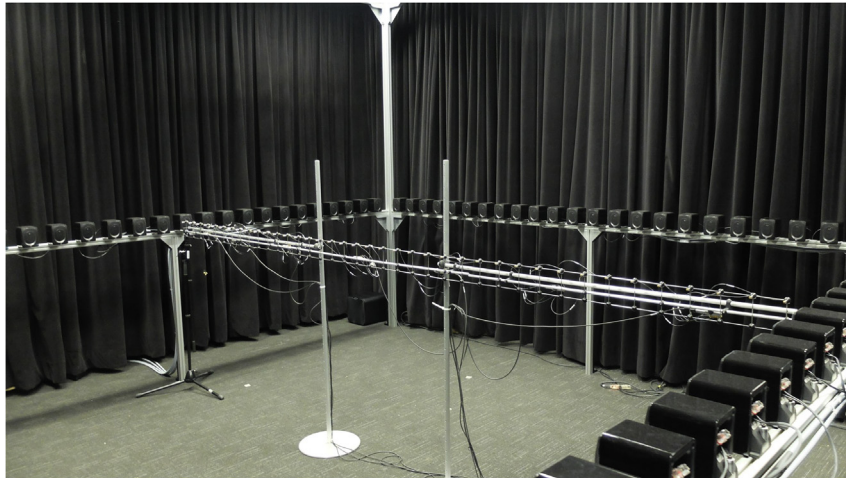


Fig. 7. WFS system and dedicated room with linear microphone array (centered linear array) for physical evaluation.

drywall covered by damping curtains. The experimental setup is shown in Fig. 7. Based on the Schroeder curve of measured impulse responses, the reverberation time is evaluated to be 166 ms. This corresponds to a relatively dry room, although with possibly more primary reflections than actual diffuse reverberation.

The time-domain driving functions D (Eq. (14)) for the physical reproduction are calculated using inverse discrete-time Fourier transform. They are played back as audio files in a digital audio workstation which drives the WFS system. Reproduced pressure signals R (Pa) are measured using a linear microphone array of $M = 39$ microphones, placed in the reproduction plane, coincident with the x axis and centered on the y axis. Microphones are equally spaced and numbered M_1 to M_{39} from $x = -1.9$ m to $x = 1.9$ m, such that microphone M_{20} is located in the center of the room at $\mathbf{x} = (0\ 0\ 0)$. The inter-microphone distance is 10 cm. Therefore, the spatial-aliasing-free frequency range for the microphone array is below 1715 Hz. The simulated time-domain signals of primary sound field P and simulated reproduction S at the microphone array shown in the results are given by inverse discrete-time Fourier transform of the frequency sampled results of Eqs. (1) and (13), respectively. This results in a time signal representing the plate impulse response at each microphone location. The P , S and R time-domain signals are then post-synchronized to produce the figures and to compensate for the global latency in the hardware signal chain.

Before conducting the experiments, the experimental setup is calibrated. First, microphones are individually calibrated according to their sensitivity measured at 1 kHz. Second, the average loudspeaker gain (frequency independent) is obtained based on impulse response measurement using the logarithmic frequency swept sine method. Based on this twofold calibration, loudspeaker signals are adjusted in gain to fit the theoretical loudspeaker model of a monopole and the raw recorded sound pressures at each microphones is converted to Pascal using the microphone sensitivities. This ensures that physical units are respected throughout the processing chain and that simulated and measured sound pressure fields can be directly compared without artificial normalization of measured data.

For each studied case, a target sound field P is first computed, a simulation of the reproduced sound field S is computed, a physically reproduced sound field R is measured and the spatial and spectral features are compared. Discrete versions of Eqs. (1), (9) and (13) are used. The simulation S is computed assuming that the secondary sources, i.e. loudspeakers, behave as omnidirectional monopoles with a flat response filtered with an 8th-order Butterworth squared high-pass filter at 120 Hz (this corresponds to the crossover frequency between the subwoofers and the loudspeakers for the WFS system) and an 8th-order Butterworth squared low-pass filter at 3891 Hz (95% of the 4096 Hz Nyquist frequency used to compute the plate response). Except when mentioned, the computed time signals P and S and the recorded signals R , are sampled at $f_s = 8192$ Hz and filtered with an 8th-order Butterworth squared low pass filter at 1000 Hz to eliminate SSD discretization artifacts from the results, where a deterioration of the physical SFR is already expected for any classical WFS experiments with this system.

7. Results of simulations and experiments

This section presents the results of simulations and experiments. First, to evaluate the proposed modified formula, few validation cases are reported for single elementary primary sources. Second, two vibroacoustic models of plates (exterior and focused) made from several thousands of elementary primary sources are reproduced in order to evaluate the performance of the method for extended primary sources with frequency-dependent directivity patterns.

The physical evaluation of the proposed sound field reproduction method is based the absolute instantaneous normalized quadratic error (dB ref 1). It takes into account both amplitude and phase of the sound pressure as function of space. The error between the target pressure field P and the theoretically reproduced sound field S is quantified by e_s , defined as:

$$e_s = 20 \log_{10} (\langle |S(\mathbf{x}, t) - P(\mathbf{x}, t)| \rangle / \langle |P(\mathbf{x}, t)| \rangle) \quad (28)$$

This metric shows the effect of the artifacts introduced by the spatial truncation and discretization of the SSD plus the 2.5D WFS approximations in idealistic free-field conditions. The error between the theoretically reproduced sound field S and the recorded reproduced sound field R is quantified by e_R , defined as:

$$e_R = 20 \log_{10} (\langle |R(\mathbf{x}, t) - S(\mathbf{x}, t)| \rangle / \langle |S(\mathbf{x}, t)| \rangle) \quad (29)$$

This metric illustrates the effect of the WFS room response and imperfections of the loudspeaker responses. By comparing the results of both metrics, one could evaluate the proposed operators and the WFS system overall performance in comparison to the target sound field. In the reported results, these instantaneous errors are smoothed by a moving average with a 15 points Hanning window applied on the numerators and denominators of Eqs. (28) and (29). This moving-average operation is denoted by $\langle \cdot \rangle$. The lower the error, the better the reproduction. For a 0 dB error, the error has the same magnitude as the reference sound field (P or S , depending on the error criterion).

7.1. Validation cases

Several cases are considered to validate the proposed modification of out-of-plane elementary primary sources. These are also used to validate the entire signal processing chain and experimental setup. Fig. 6(a) and (b) presents the validation cases. First, in-plane elementary sources are studied in Fig. 6(a). Then, out-of-plane primary sources are considered for the configuration shown in Fig. 6(b). The source signals for these validation cases are Gaussian pulses with a 600 Hz center frequency and a 0.5 fractional bandwidth. Furthermore, a 263-sample delay is introduced between the center and left point sources to distinguish

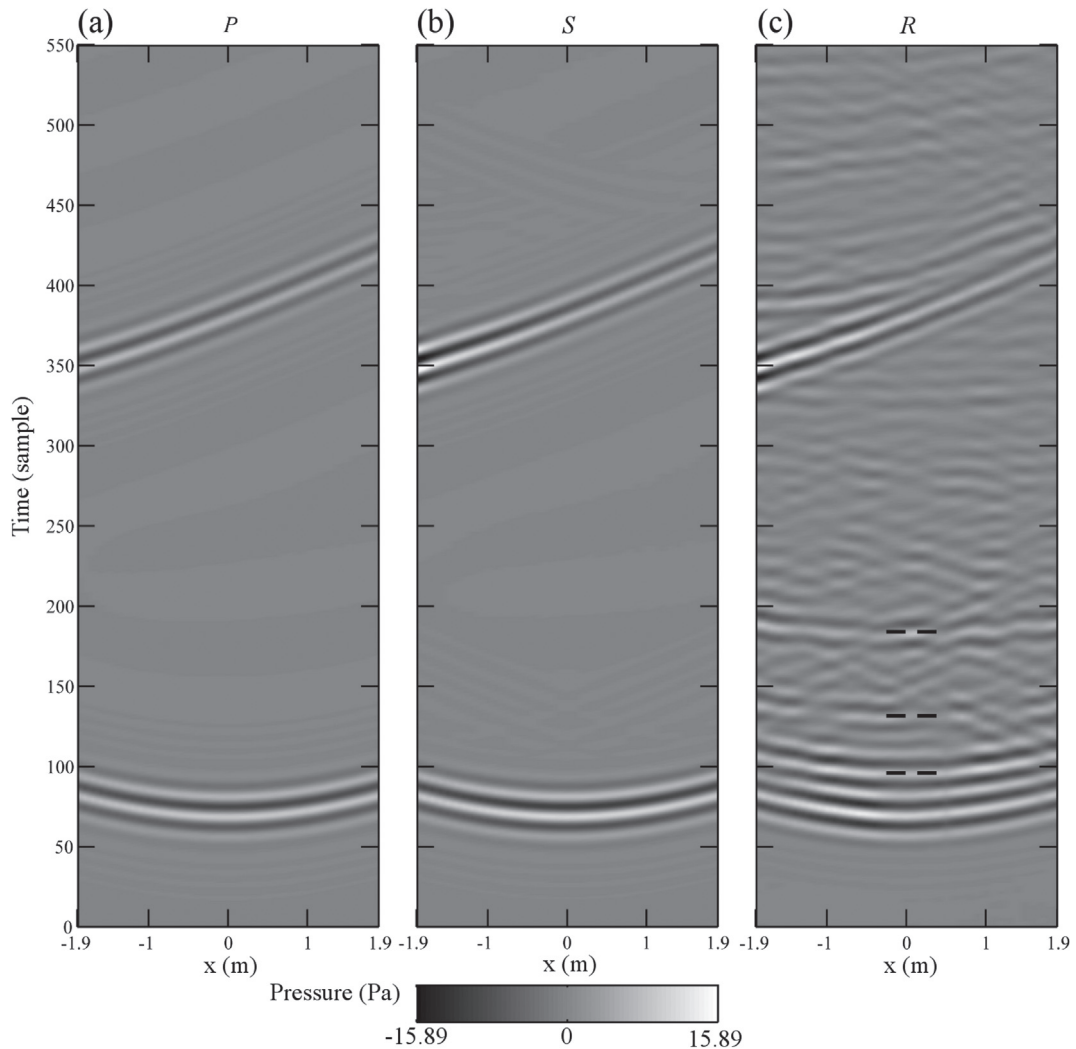


Fig. 8. Time plot of pressure sound fields (a) $P(\mathbf{x}, t)$, (b) $S(\mathbf{x}, t)$ and (c) $R(\mathbf{x}, t)$ for the in-plane test case, at the microphone array along x . The thick black dashed lines indicate the room reflections for the first pulse in this order: 1) floor and back wall, 2) ceiling, and 3) control desk.

the corresponding wavefronts.

Fig. 8 shows the target, reproduced and measured sound fields at the microphone array for the in-plane test case. Fig. 9 shows the corresponding errors. The error plots allow identifying which parts in time are appropriately reproduced. White zones in error plots indicate that the magnitude of the error is the same or greater than the target sound field. Dark zones indicate that the magnitude of the error is less than the target sound field. The reader should note that the error metric is meaningless between pulses since it involves a division by zero since the target field is silent between pulse: Errors are expected to be high between experimentally reproduced wavefronts. As one can note based on free-field simulations S , the first wavefront is correctly reproduced at the linear microphone array. For the second wavefront, the reproduction is less accurate for x approaching -2 and 2 . However, this is expected behavior since in that case, the linear microphone array is no longer aligned with the reference line. Finally, the measured reproduced sound field shows that the desired sound field is reproduced with the supplementary room response. To further highlight the room effect, the expected arrival time for the early reflection are shown for the floor, the back wall, the ceiling and the control desk as thick dashed lines for the first wave front.

Similar results are provided for the case of out-of-plane primary sources in Figs. 10 and 11. Similar conclusion applies for the reproduction of incoming direction in the horizontal plane. However, one notes that the simulated reproduction is more accurate around the center of the microphone array. This is the consequence of the out-of-plane compensation factor Q_c . When spherical waves are emitted out-of-plane by an elementary primary source, the projected wavelength on the reproduction plane is not the same as the in-plane wavelength emitted by the secondary sources. This is not something audible *per se*, but this is visible in objective results: the target and reproduced amplitudes and phases only match on the reference line. This is so even when SPA is used, contrary to the in-plane test case where amplitudes match only on the reference line and phases match everywhere. Although the phase errors may seem therefore problematic, it is reminded that it is a consequence of reducing the third dimension and one should keep in mind that the in-plane directions of arrival are, however, properly reproduced. Therefore, albeit not providing a perfect sound field reproduction, these results validate the compromise represented by the related technological choices.

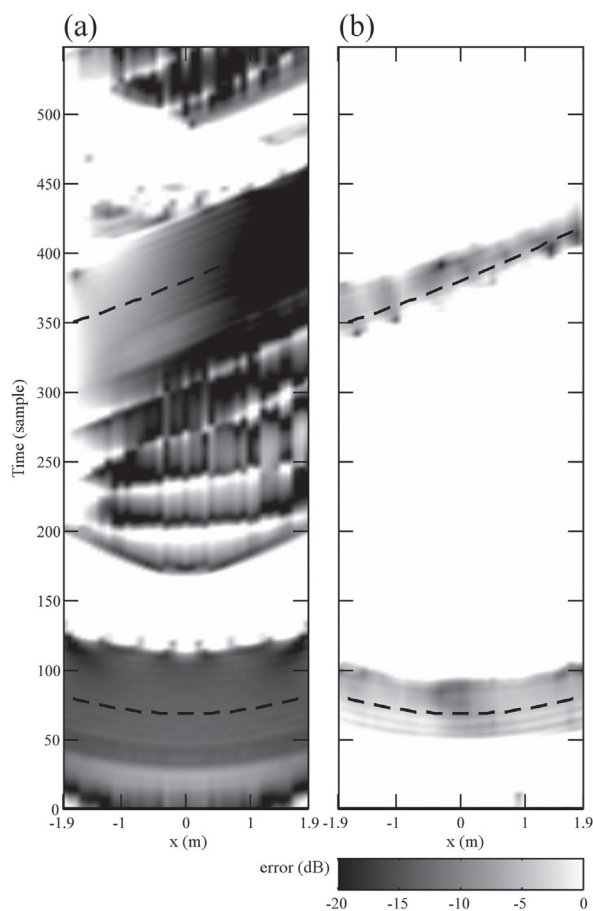


Fig. 9. Error plots (a) e_s and (b) e_R (dB ref 1) for the in-plane test case, at the microphone array along x . The thick black dashed lines indicate each pulse's wavefront peak, given as a time reference.

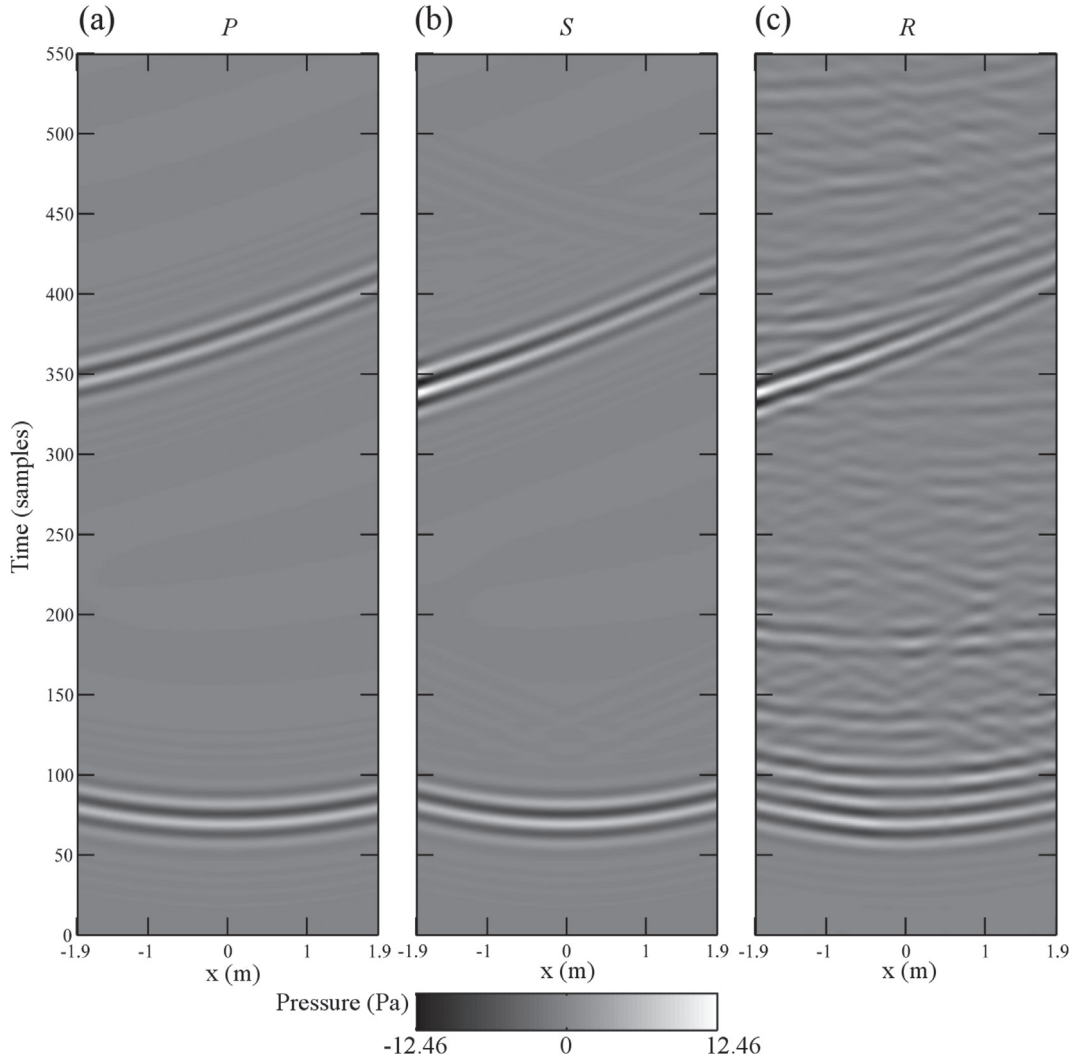


Fig. 10. Time plot of pressure sound fields (a) $P(\mathbf{x}, t)$, (b) $S(\mathbf{x}, t)$ and (c) $R(\mathbf{x}, t)$ for the out-of-plane test case, at the microphone array along x . The thick black dashed lines indicates the room reflections.

Further verifications for the out-of-plane elementary primary source is reported in Fig. 12. In this figure, the error e_s evaluated at origin (i.e. on the reference line) is shown as function of frequency and elementary primary source height z_s for three in-plane distances (at $y_s = 3, 4$ and 8 m, with $x_s = 0$). For most of cases, the reproduction errors are significantly below 0 dB ref 1 (except for the low-frequency range and for low z_s in Fig. 12(a)). For instance, for the case show in Fig. 12(b), the average error e_s is -14.1 dB ref 1. Also, it should be noted that as z_s increases the error in fact decreases. In fact, the error decreases to a notch (around 7 m in Fig. 12(b)). As the primary source is further away in the horizontal plane, this reproduction error notch is also pushed towards larger z_s . Accordingly, based on these results, it is concluded that the proposed method offers an acceptable reproduction error reduction for a point on the reference line even for primary sources with $z_s \neq 0$. Finally, in order to evaluate the reproduction outside the reference line, Fig. 13 shows the normalized amplitude-only error as function of frequency and as function of listening position y (with $x = 0$). In this case, the amplitude-only error is considered since the error, including phase error, would not be representative outside the reference line since the in-plane reproduced wavelength is different from the in-plane target wavelength for an out-of-plane elementary primary source. As expected, the amplitude-only reproduction error is higher than for the previous figure. Also, there is a notch of amplitude-error at fixed distances from the loudspeaker array. At these specific distances, the amplitudes of the reproduced and target wave fronts are nearly equals. Otherwise, the reproduced amplitude is stronger than the target amplitude for distances smaller than that distance, and vice versa. As a concluding remark on this matter, it should be keep in mind that for an extended primary source as studied in this paper, there is many elementary primary sources: each having a different reference line, each having a different error distribution. Therefore, it is expected that such out-of-plane errors are spread differently and combined in a mixture of the simple cases reported in this section.

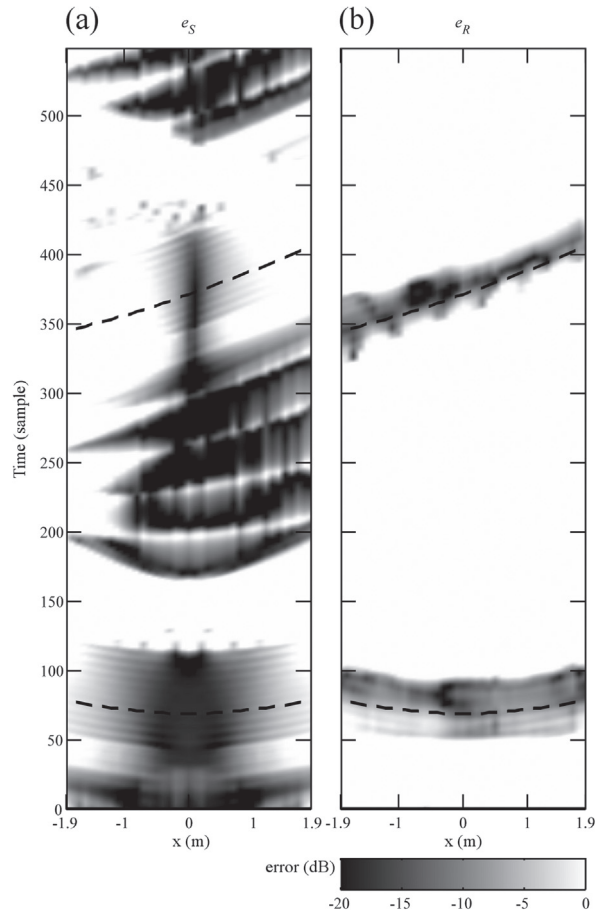


Fig. 11. Error plots (a) e_S and (b) e_R (dB ref 1) for the out-of-plane test case, at the microphone array along x . The thick black dashed lines indicate each pulse's wavefront peak, given as a time reference.

7.2. Exterior plate

Fig. 14 shows the target, reproduced and measured sound fields at the microphones, for the exterior plate with characteristics provided in Table 1. The position of the exterior plate, relative to the loudspeaker array, is shown in Fig. 6. From Fig. 14 (a), one visualizes the target sound field as radiated by the plate excited by an impulse point force. First, a spherical-like wavefront radiates from the plate: This spherical wave emerges from the excitation position on the plate. After the passage of this first wavefront, the propagating waves and modal patterns in the plate radiate in multiple directions. Between the first wavefront

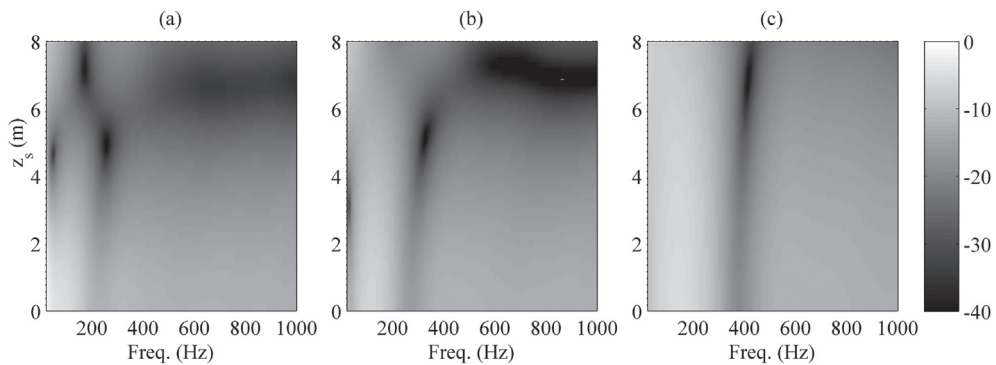


Fig. 12. Error plots e_S (dB ref 1) at origin as function of frequency and elevation z_s , of an out-of-plane elementary primary source at: (a) $x_s = (0, 3, 0 \dots 8)$ m, (b) $x_s = (0, 4, 0 \dots 8)$ m, (c) $x_s = (0, 8, 0 \dots 8)$ m.

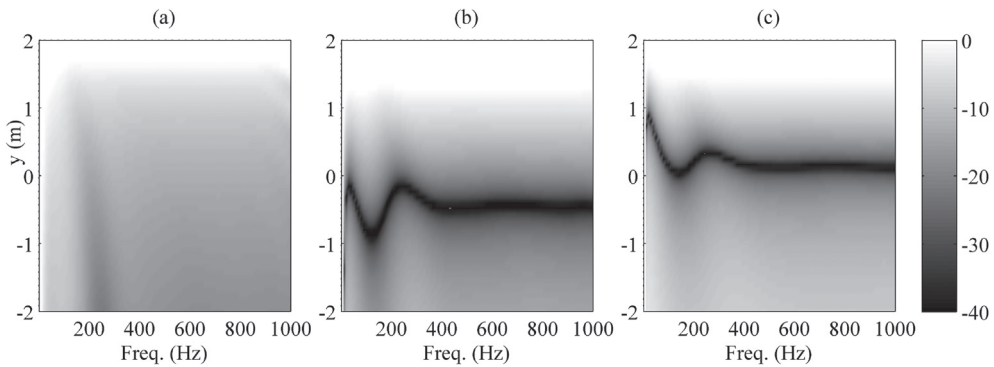


Fig. 13. Normalized amplitude error (dB ref 1) as function of distance along y (for $x = 0$) frequency for three elevations z_s of an in-plane and out-of-plane elementary primary source at: (a) $\mathbf{x}_s = (0, 3, 0)$ m, (b) $\mathbf{x}_s = (0, 3, 4)$ m, (c) $\mathbf{x}_s = (0, 3, 8)$ m.

and these radiated components (marked by a less distinct second wavefront), little radiation is observed for approximately 30 samples. This is due to the greater acoustic propagation distance between the boundaries of the plates (which are the main components of sound radiation, i.e. edge and corner modes [37]) and the microphone array, compared to the distance between the point force excitation and the microphone array.

On this matter, one notes in Fig. 14 two dominating wavefront curvatures that are repeated in the space-time plot. They are visually identified by thick black dashed curves in the left pane. These specific patterns in the $P(\mathbf{x}, t)$ plot have the same curvature as spherical or cylindrical waves emerging from the vertical boundaries of the plate. This shows that, as expected from sound radiation of plates, edge and corner modes are the dominating modes of sound radiation in the aliasing-free frequency range of interest and for plate models of this size [37]. This justifies and demonstrates the usefulness of the approach reported in this paper for the description of an extended primary vibrational source as a dense elementary primary source grid in comparison with methods based on monopole localized on antinodes of a single normal mode shape [26]. The corresponding simulated reproduced sound field $S(\mathbf{x}, t)$ is shown in Fig. 14 (b). It is in good agreement with the target. Although the reproduced and target fields have several minor differences in wavefront amplitude and time of arrival, the main features, including time and space distributions, are well reproduced and hence confirming the validity, in terms of spatial attributes, of the proposed method, 2.5D adaptation, and correction factors.

The measured reproduced sound field is shown in Fig. 14 (c). Besides the expected room response, one notes that the spatial features of the target field are present in the experimentally reproduced sound field. On the one hand, according to the precedence effect [32], these room reflections and reverberations that follow the direct sound should not too much alter the spatial localization of the plate. In all cases, any spatial sound reproduction technology would suffer from such room effect on spatial perception, i.e. it is not specific to the proposed method of extended source reproduction. On the other hand, the room may alter the perceived spectrum. Accordingly, in order to evaluate the reproduction quality as a function of frequency, the vibroacoustic system (force - plate - sound radiation - sound reproduction) frequency response functions (FRF) at microphone M_{20} over the frequency range below the SSD aliasing frequency are shown in Fig. 15. One notices that the simulated reproduced sound field has a response very similar to the target FRF, and that the frequency domain features are recreated. Most notably, the peak amplitudes (corresponding to plate damped resonant frequencies) are similar. Small deviations between the target and simulated reproduced sound fields exist between neighboring damped resonant frequencies.

The experimentally reproduced frequency response functions show a modal behavior and signature essentially similar to the target, with more important deviations for off-resonance frequencies. Since on-resonance levels are in average about 15 dB larger than off-resonance levels, errors between resonant frequencies should not much affect the perceived frequency content. This should be verified by formal listening tests. In all cases, the frequency domain features of the model are recreated.

According to these observations of the FRFs, the proposed method is theoretically able to recreate the spectral signature of the extended primary source. As expected, the actual WFS system (amplifiers, loudspeakers and, especially, the room response) degrades the FRF, but the prominent features are still reproduced. Note that the spectrum deviation below 130 Hz is mostly created by the low-end limitation of the loudspeakers. This can be palliated by the use of subwoofers.

7.3. Focused plate

Fig. 16 shows the target, reproduced and measured sound fields at the microphone array for the focused plate. The position of the focused plate, relative to the loudspeaker array, is shown in Fig. 6.

One can see in Fig. 16 (a) the first distinct wavefront from the impulse excitation. The wavefront diagonal patterns are different to the exterior plate, because of the different orientation θ_s , but they still originate from the vertical linear boundaries of the plate. In Fig. 16 (b) and (c), one can see that the focused reproduction add artifacts before the first wavefront (this is caused by the focused nature of the primary source [32]), especially on the left of the plot, which is very close to the active

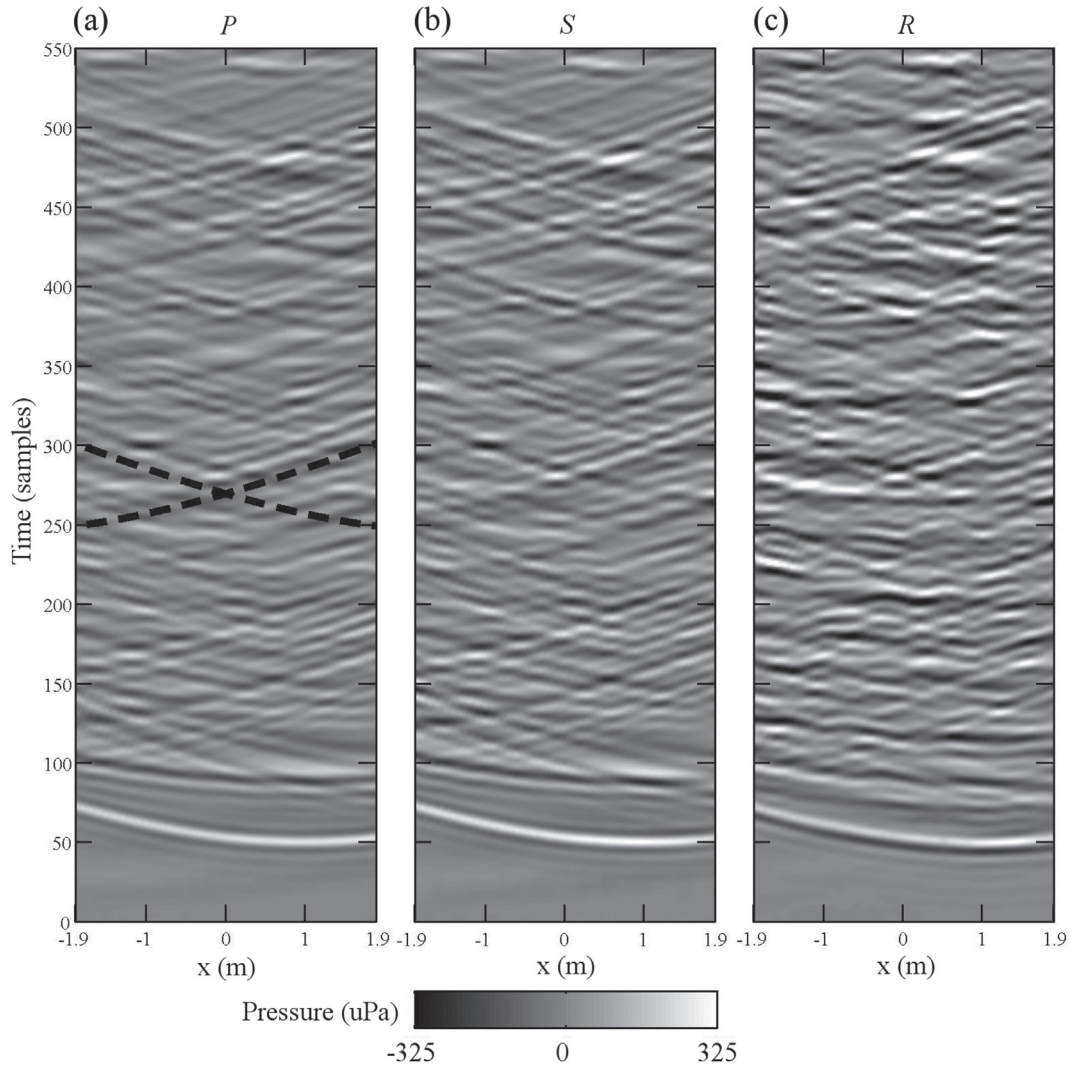


Fig. 14. Time plots of instantaneous sound pressure fields (a) P , (b) S and (c) R for the exterior plate, at the microphone array. Only the first 550 samples of the responses are shown. The two thick black dashed lines in the left pane indicate the two dominating typical wavefront curvatures as seen at the microphone array. They correspond to spherical or cylindrical waves coming from the vertical boundaries of the plate.

loudspeakers. However, although the reproduced and target fields have several minor differences in amplitude and timing, the main features, including time and space distributions, are well reproduced. Also, informal listening tests confirm the perception of an extended focused primary source in the listening space.

The focused plate frequency response functions at M_{20} are shown in Fig. 17. These results confirm the previous observations on the reproduced spectrum with better clarity. Indeed, due to the fact that the focused plate is of smaller extent than

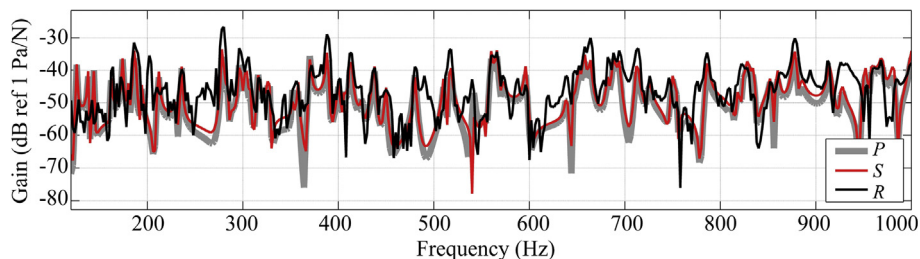


Fig. 15. Frequency response functions $P(\mathbf{x}_{20}, \omega)/F(\omega)$, $S(\mathbf{x}_{20}, \omega)/F(\omega)$ and $R(\mathbf{x}_{20}, \omega)/F(\omega)$ for the exterior plate, at M_{20} .

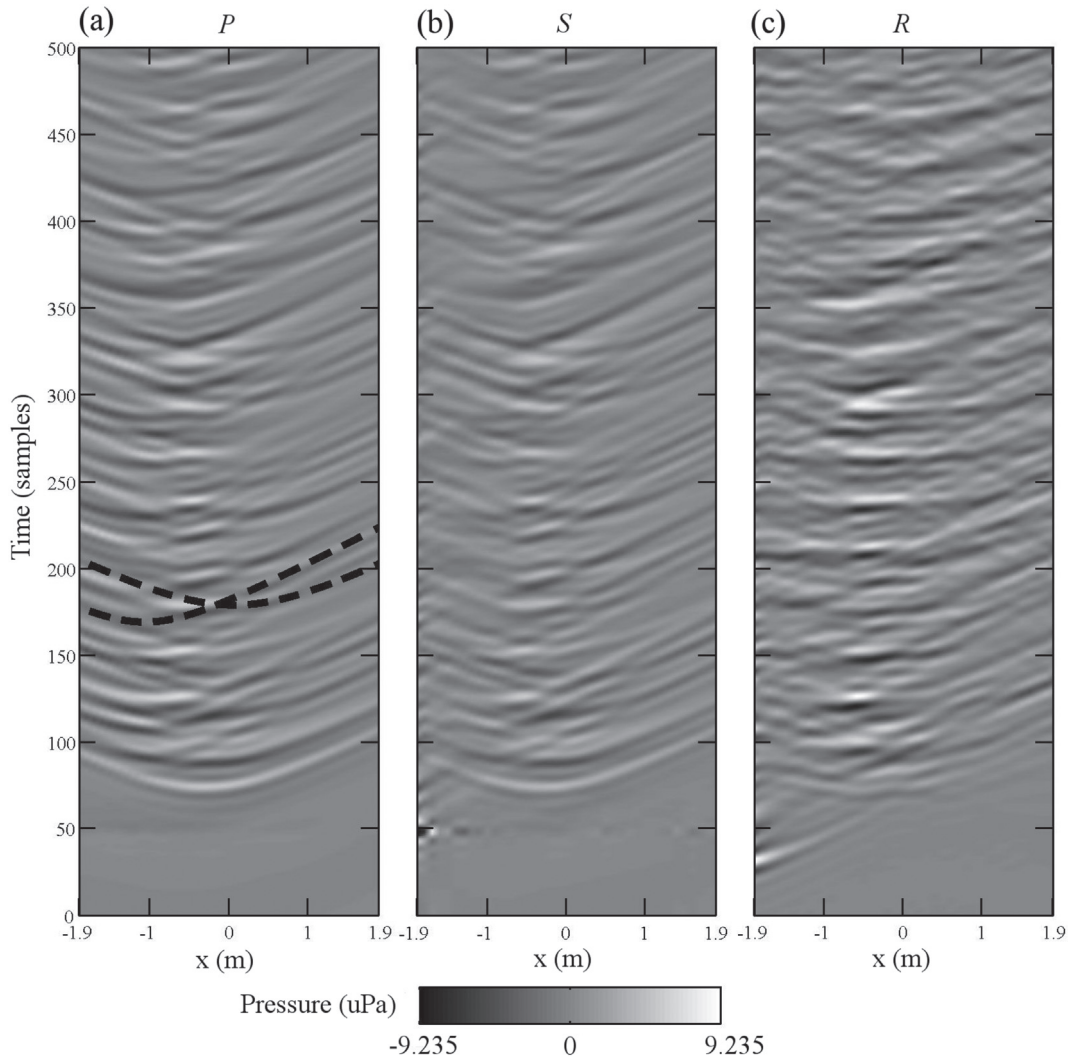


Fig. 16. Time plots of instantaneous sound pressure fields (a) P , (b) S and (c) R for the focused plate, at the microphone array. Only the first 550 samples of the responses are shown. The two thick black dashed lines in the left pane indicate the two dominating typical wavefront curvatures as seen at the microphone array. They correspond to spherical or cylindrical waves coming from the vertical boundaries of the plate.

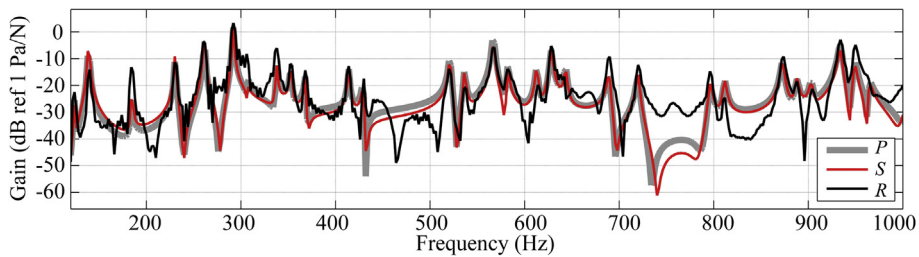


Fig. 17. Frequency response functions $P(\mathbf{x}_{20}, \omega)/F(\omega)$, $S(\mathbf{x}_{20}, \omega)/F(\omega)$ and $R(\mathbf{x}_{20}, \omega)/F(\omega)$ for the focused plate, at M_{20} .

the exterior plate, the modal density is lower for the tested frequency range. From this figure, one notes the match of the main frequency domain features between P , R and S . The small deviations between P and S show that even if more reproduction artifacts are present, due to the elementary primary sources being focused, the resulting spectrum of the extended primary source is still reproduced, and the deviations are mainly due to the room effects and measurement noise in the case of experimental validations.

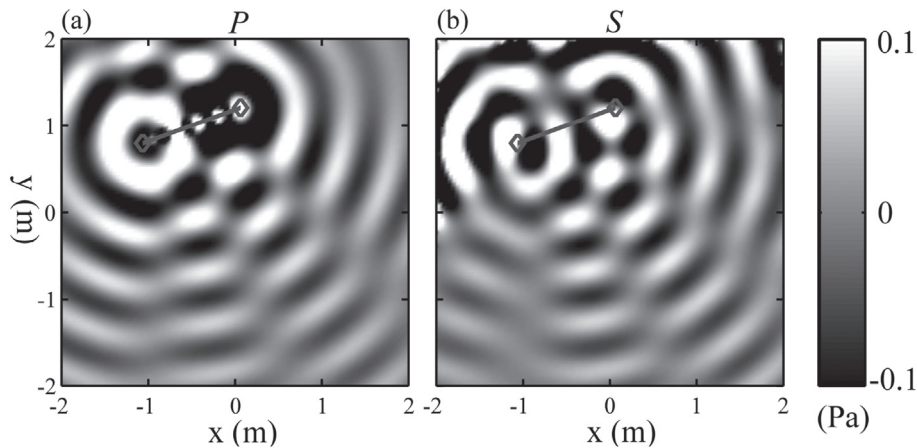


Fig. 18. Real parts of complex sound pressure fields (a) P and (b) S at 608 Hz (mode 7–3) for the focused plate. The plate is shown as a thick gray line with markers at its vertical boundaries.

For a focused plate, it is more difficult to fully visualize the spatial representations of the target and reproduced sound fields with space-time representations such as in Fig. 16. Therefore, Fig. 18 is introduced to show the spatial (x - y) distribution of the real part of the complex sound pressure fields P and S at the eigenfrequency 608 Hz of mode 7–3 for the focused plate. Since R is based on a linear microphone array measurement, it is not shown in this case.

Several observations can be drawn from the target sound field P : 1) there are evanescent waves in the close proximity of the plate and 2) there are four main radiation lobes in front of the plate, with alternating polarity. One can verify that for this spatial-aliasing-free frequency, the directivity pattern of propagating components are appropriately reproduced: Amplitudes and phase shifts of directivity lobes are well reproduced. However, as expected, the evanescent waves are not recreated and converging waves exist behind the focused plate: only a region inside the SSD is considered as a valid reproduction area. This is coherent with the secondary source selection criterion described in Section 4.5.

8. Illustrative engineering application

The driving interest for this work was stated as to use mechanical engineering analytical or numerical models to drive virtual auditory displays in an acoustical product or sound quality design workflow. As an example, a virtual measurement setup imitation of the one used for Transmission Loss (TL) measurement of a panel can be achieved using the proposed approach. This problematic is clearly emerging as a future trend in sound quality research. Indeed, if sound quality investigations are now common for products or devices (cars, vacuum cleaner) where the source and filter are studied as a whole, application of sound quality principles and methodology represents significant challenges and opportunities since subject under study no longer includes the source. In this trend, the work presented in this paper would allow for the auralization and rapid comparison of the sound transmitted through different panels. Typically, TL measurement is performed by acousticians to measure the frequency-dependent sound attenuation when diffuse sound field is transmitted through a partition. In experimental situations, the partition is mounted between a reverberant room, where a known broadband diffuse pressure field is created to excite the entire surface of the partition, and an anechoic room, where transmitted active sound intensity is measured. Based on the ratio of impinging energy to radiated sound intensity, one can obtain the frequency-dependent or per- n^{th} -octave-bands TL in dB. Also, using the proposed method, one could auralize an Insertion Loss (IL) measurement by: 1) Reproducing a diffuse sound field going through an aperture and 2) virtually inserting a panel in the aperture, so that the transmitted sound is filtered by the panel response, and 3) reproducing the resulting transmitted sound field including space and frequency features.

In these typical and standardized measurements scenarios, on-site pairwise listening tests of two different panels for sound quality purposes are never, to the authors' knowledge, performed. This is because: 1) the installation time is prohibitive for comparison based on listening, 2) only one panel can be mounted at the time and 3) the infrastructure cost is high. Based on this, pairwise listening tests could only be performed with binaural or stereo sound reproductions of measured sound fields in front of partitions. However, this would not faithfully transmit the actual spatial distribution of sound which may influence auditory masking. The proposed method circumvents this issue. It can be implemented in two distinct ways that illustrate the application potential of the method: 1) using numerical vibroacoustic models as the generator for the velocity field of the extended primary source and 2) using measured velocity fields obtained by, for instance, laser vibrometers or acoustical near-field holography [28].

In order to illustrate the approach in a situation that is representative of an engineering context, a final example is provided. Instead of an impulsive point force excitation, a 3D diffuse and broadband (0–4096 Hz, with uniform amplitude and frequency resolution of 2 Hz) sound pressure field was simulated [36,38] and used to acoustically excite one side of a baffled plate, to simulate a TL measurement. Therefore, this case includes supplementary physical phenomena such as coincidence. Fig. 19 shows

the target, reproduced and measured sound fields at the microphone array. It corresponds to the sound field transmitted through a $1.2 \times 0.8 \times 0.003$ m aluminum plate, with the plate centroid at $\mathbf{x}_c = (0 \ 2.5 \ 0)$ m (as an extended exterior source), with $\theta_s = 180^\circ$, $L_s = 151$ and $H_s = 101$. One observes that the proposed WFS operators still perform adequately based on recreated spatial features, even for a plate excited by an spatially-extended diffuse sound field and not a single point force as reported in the earlier sections.

The resulting frequency spectra at M_{20} are shown in Fig. 20. The average levels are correctly reproduced. The simulated case shows that the method theoretically perform very well in terms of reproduced spectra and that frequency domain features are reproduced with great details. Indeed, despite a slight offset, the overall spectral shape is well reproduced. The dominating degradation is caused by the actual room and loudspeakers used for the experiments. Again, in Figs. 19 (c) and 20, one can observe that room effects distort the physical reproduction and constructive/destructive interferences alter the reproduced spectra. It is important to remind that reproduction simulations were carried in a free-field environment. Also, if an actual aluminum plate was installed in the WFS room, the room effects would also affect the plate sound field radiation, as it affects the reproduced sound field.

Since the plate response is computed with a broadband diffuse field acting over its entire back side, it is possible to apply a posteriori an excitation signal spectrum. Indeed, as an applied example, one could multiply in frequency domain a given acoustical field excitation spectrum and the broadband driving functions in order to simulate any kind of acoustic excitation as diffuse sound field. An illustrative example would be the reproduction of an urban recorded sound transmitted through a virtual window, or through a vehicle panel. This is especially relevant for the development of sound quality within the field of building acoustics using virtual acoustics.

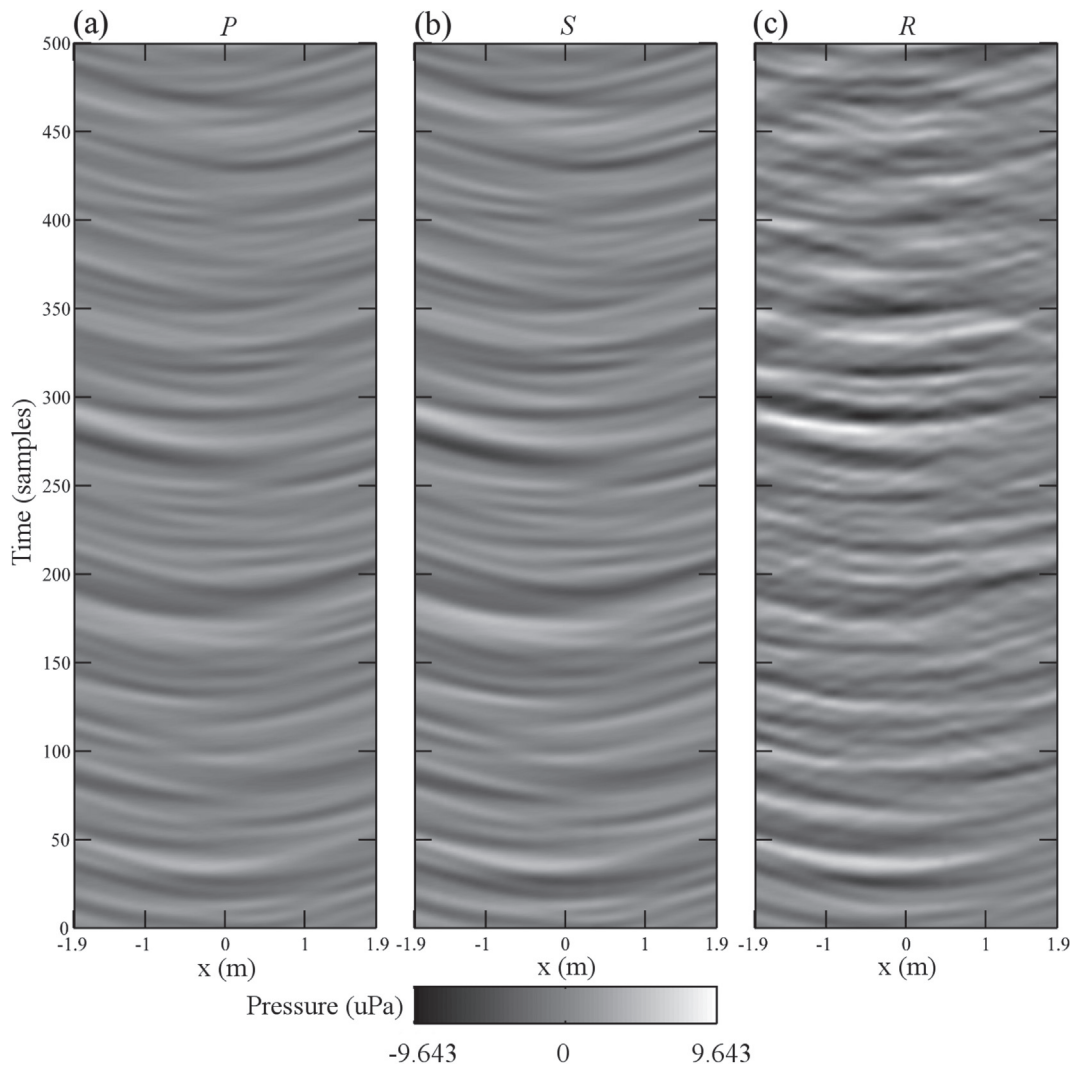


Fig. 19. Time plots of instantaneous sound pressure fields (a) P , (b) S and (c) R (at the microphone array, along x) for the sound field transmitted through a plate subject to diffuse sound field excitation. Excerpts of 61 ms are shown.

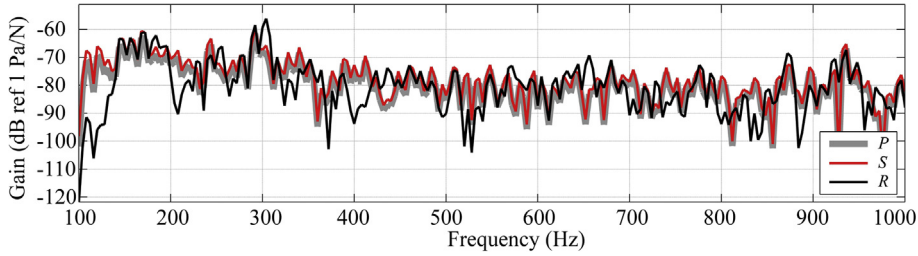


Fig. 20. Frequency spectra at M_{20} $P(\mathbf{x}_{20}, \omega)$, $S(\mathbf{x}_{20}, \omega)$ and $R(\mathbf{x}_{20}, \omega)$ for the transmitted sound through a plate subject to diffuse sound field excitation.

9. Conclusion

A method to use vibroacoustics engineering models to drive virtual auditory displays with 2.5D Wave Field Synthesis and piecewise loudspeaker arrays was proposed. The WFS operator is compatible with focused and exterior spatially-distributed primary sources, and compensates for out-of-plane elementary primary sources. In this paper, a discretized and extended thin plate model was used to illustrate and evaluate the overall performance of the operator with time and frequency domain data. Simulations demonstrated that the model spectral and spatial characteristics, such as trace plots of instantaneous sound pressure field at a linear microphone array, are reproduced in the horizontal plane with the proposed operators. Experimental measurements of reproduced sound fields have shown that direct sound is well reproduced and that room effects degrade the physical reproduction, though they are still acceptable for practical applications where the room is expected to have a response. Based on reported results, it is also concluded that further in-depth studies of out-of-plane primary is required. Such studies should include parametric comparisons of different modifications for out-of-plane primary sources. Future work should also investigate the perception of the proposed method through formal listening tests.

Acknowledgement

The authors would like to thank Pierre Lecomte and Yann Pasco for their help and comments. This work was supported by grants from the Natural Sciences and Engineering Research Council of Canada, the Fonds de recherche du Québec - Nature et technologies, the Université de Sherbrooke Engineering Faculty and the Center for Interdisciplinary Research in Music, Media, and Technology. The construction and acquisition of the WFS system was possible through a Canada Foundation for Innovation, New Initiatives Fund, project 19969.

Appendix Stationary phase approximation for out-of-plane elementary primary sources

The Stationary Phase Approximation (SPA) is used for integrals of the following form (as in Eq. (3)) [28]:

$$I = \int_{-\infty}^{\infty} f(z_0) e^{j\Psi(z_0)} dz_0. \quad (30)$$

For the studied case, one finds

$$S = -\zeta \frac{j\omega\rho_0}{(2\pi)^2} \int_{x_0} \int_{A_s} u_s \int_{z_0} \frac{e^{-jk(r-\zeta r_0)}}{rr_0} \left(\frac{1}{r_0} - \zeta jk \right) \cos(\phi) \cos(\beta) dz_0 dx_s dz_s dx_0, \quad (31)$$

$$S = -\zeta \frac{j\omega\rho_0}{(2\pi)^2} \int_{x_0} \int_{A_s} u_s I(z_0) dx_s dz_s dx_0, \quad (32)$$

with

$$I = \int_{z_0} \frac{e^{-jk(r-\zeta r_0)}}{rr_0} \left(\frac{1}{r_0} - \zeta jk \right) \cos(\phi) \cos(\beta) dz_0, \quad (33)$$

so that

$$f(z_0) = \frac{\cos(\phi) \cos(\beta)}{rr_0} \left(\frac{1}{r_0} - \zeta jk \right), \quad (34)$$

and

$$\Psi(z_0) = -k(r - \zeta r_0). \quad (35)$$

Note that $r = \|\mathbf{r}\| = \|\mathbf{x}_0 - \mathbf{x}\|$. Therefore, z_{SP} is the stationary phase point along z_0 for which, one finds:

$$\left. \frac{\partial \Psi(z_0)}{\partial z_0} \right|_{z_0=z_{SP}} = k \left(\frac{z - z_{SP}}{r_p} + \zeta \frac{z_{SP} - z_s}{r_{SP}} \right) = 0, \quad (36)$$

with

$$r_p = \|\mathbf{r}_p\| = \|\mathbf{x} - \mathbf{x}_{SP}\|, \quad (37)$$

and

$$r_{SP} = \|\mathbf{r}_{SP}\| = \|\mathbf{x}_{SP} - \mathbf{x}_s\|. \quad (38)$$

Then the SPA gives [28]

$$I \approx I(z_{SP}) = f(z_{SP}) e^{i\Psi(z_{SP})} \sqrt{\frac{-\zeta 2\pi j}{\partial^2 \Psi(z_{SP}) / \partial z_{SP}^2}}. \quad (39)$$

From Eq. (35), it is obvious that the phase will be stationary for any frequency for the shortest distance ($r - \zeta r_0$). Therefore, for a given elementary primary source and a given secondary source, the stationary phase point will always lie above or below \mathbf{x}_0 at z_{SP} when \mathbf{r}_0 is collinear with \mathbf{r} . For a problem with elementary primary sources in the horizontal plane and an horizontal listening plane, $z = 0$ and $z_s = 0$, Eq. (36) gives:

$$0 = \frac{z_{SP}}{r_p} + \frac{\zeta z_{SP}}{r_{SP}} = z_{SP} \left(\frac{1}{r_p} + \frac{\zeta}{r_{SP}} \right) \quad (40)$$

Then one readily obtains:

$$z_{SP} = 0 \quad (41)$$

For problem with elementary primary sources outside the horizontal plane, but with the listening area still defined as an horizontal plane, one finds from Fig. 4 and by similar triangles properties:

$$z_{SP}(\mathbf{x}_0, \mathbf{x}_s) = z_s \frac{\gamma + \zeta \|\mathbf{x}_0 - \mathbf{x}_s\| \Big|_{z_s=0}}{\gamma} \quad (42)$$

as reported in Eq. (17) (γ is defined in Eq. (10)).

References

- [1] K. Gösele, E. Schröder, Sound insulation in buildings, in: G. Müller, M. Möset (Eds.), Handbook of Engineering Acoustics, Springer, Berlin, 2013, pp. 137–164.
- [2] J. Blauert, U. Jekosch, Sound-quality evaluation - a multi-layered problem, *Acust. Acta Acust.* 83 (1997) 747–753.
- [3] U. Jekosch, Basic concepts and terms of quality, reconsidered in the context of product-sound quality, *Acta Acustica united Acustica* 90 (2004) 999–1006.
- [4] A. Nykänen, Methods for Product Sound Design, Ph.D. thesis, Lulea University of Technology, Lulea, Sweden, 2008.
- [5] W. Keiper, Sound quality evaluation in the product cycle, *Acust. Acta Acust.* 83 (1997) 784–788.
- [6] N. Tsingos, Using programmable graphics hardware for auralization, in: Presented at the EAA Symposium on Auralization, Espoo, Finland, 2009.
- [7] M. Noisternig, B.F.G. Katz, S. Siltanen, L. Savioja, Framework for real-time auralization in architectural acoustics, *Acta Acustica united Acustica* 94 (2008) 1000–1015.
- [8] M. Vorländer, Auralization: Fundamentals of Acoustics, Modelling, Simulation, Algorithms and Acoustic Virtual Reality, Springer, Berlin, 2008.
- [9] S. Siltanen, T. Lokki, S. Kiminki, L. Savioja, The room acoustic rendering equation, *J. Acoust. Soc. Am.* 122 (2007) 1624–1635.
- [10] P.T. Calamia, B.E. Markham, U.P. Svensson, Diffraction culling for virtual-acoustic simulations, *Acta Acustica united Acustica* 94 (2008) 907–920.
- [11] K. Kowalczyk, M. van Walstijn, Formulation of locally reacting surfaces in FDTD/K-DWM modelling of acoustic spaces, *Acta Acustica united Acustica* 94 (2008) 891–906.
- [12] E. Stavrakis, N. Tsingos, Topological sound propagation with reverberation graphs, *Acta Acustica united Acustica* 94 (2008) 921–932.
- [13] J. Durany, P. Arumi, A. Garriga, R. Mateos, Sound spatialization using ray tracing, in: Proc. of the EAA Symposium on Auralization Espoo, Finland, June 2009.
- [14] J.H. Rindel, C.L. Christensen, Auralization of a symphonic orchestra with odeon - the chain from musical instruments to the eardrums, in: Proc. of the EAA Symposium on Auralization Espoo, Finland, June 2009.
- [15] K. Hochgraf, J. Botts, N. Xiang, J. Braasch, Simulation and auralization of a concert hall's inhomogeneous sound field using finite difference time-domain methods and wave field synthesis, in: Program Abstracts of the 169th Meeting of the Acoustical Society of America, Pittsburgh, USA, May 2015.
- [16] G. Kearney, C. Masterson, S. Adams, F. Boland, Towards efficient binaural room impulse response synthesis, in: Proc. of the EAA Symposium on Auralization, Espoo, Finland, June 2009.
- [17] M. Aretz, R. Nöthen, M. Vorländer, D. Schröder, Combined broadband impulse responses using FEM and hybrid ray-based methods, in: Proc. of the EAA Symposium on Auralization, Espoo, Finland, June 2009.
- [18] N. Raghuvanshi, B. Loyld, N.K. Govindaraju, M.C. Lin, Efficient numerical acoustic simulation on graphics processors using adaptive rectangular decomposition, in: Proc. of the EAA Symposium on Auralization, Espoo, Finland, June 2009.
- [19] U.P. Svensson, U. Reiter, D.M. Behne, Evaluating auralization, in: Proc. of the EAA Symposium on Auralization, Espoo, Finland, June 2009.
- [20] F. Wefers, D. Schröder, Real-time auralization of coupled rooms, in: Proc. of the EAA Symposium on Auralization, Espoo, Finland, June 2009.
- [21] S. Spors, H. Wierstorf, A. Raake, F. Melchior, M. Frank, F. Zotter, Spatial sound with loudspeakers and its perception: a review of the current state, *Proc. IEEE* 101 (2013) 1920–1938.
- [22] A. Bolduc, P.-A. Gauthier, T. Ramanana, A. Berry, Sound field reproduction of vibroacoustic models: application to a plate with wave field synthesis, in: Presented at the AES 55th Conference on Spatial Audio, Helsinki, Finland, 2014.
- [23] E. Start, Direct Sound Enhancement by Wave Field Synthesis, Ph.D. thesis, Delft University of Technology, Delft, The Netherlands, 1997.

- [24] E. Verheijen, Sound Reproduction by Wave Field Synthesis, Ph.D. thesis, 2nd Edition, Delft University of Technology, Delft, The Netherlands, 2010.
- [25] P. Cook, Real Sound Synthesis for Interactive Applications, A K Peters, Natick, 2002.
- [26] J. Ahrens, S. Spors, Two physical models for spatially extended virtual sound sources, in: Presented at the AES 131st Convention, New York, United States, 2011.
- [27] M. Baalman, On Wave Field Synthesis and Electro-acoustic Music, with a Particular Focus on the Reproduction of Arbitrarily Shaped Sound Sources, Ph.D. thesis, Berlin University of Technology, Berlin, Germany, 2008.
- [28] E.G. Williams, Fourier Acoustics: Sound Radiation and Nearfield Acoustical Holography, Academic Press, San Diego, 1999.
- [29] M. Junger, D. Feit, Sound, Structures, and Their Interaction, 2nd Edition, The MIT Press, Cambridge, 1986.
- [30] S. Spors, R. Rabenstein, J. Ahrens, The theory of wave field synthesis revisited, in: Presented at the AES 124th Convention, Amsterdam, Netherlands, 2008.
- [31] A.J. Berkhout, D. De Vries, P. Vogel, Acoustic control by wave field synthesis, *J. Acoust. Soc. Am.* 93 (1993) 2764–2778.
- [32] J. Ahrens, Analytical Methods of Sound Field Synthesis, Springer, Berlin, Germany, 2012.
- [33] A. Bolduc, Reproduction sonore de modèles vibroacoustiques 3D de plaques par Wave Field Synthesis [Sound reproduction of 3D plate vibro-acoustics models by Wave Field Synthesis], M.Sc.A thesis, Université de Sherbrooke, Sherbrooke, Canada, 2015.
- [34] M. Baalman, Elevation problems in the auralisation of sound sources with arbitrary shape with wave field synthesis, in: Presented at the International Computer Music Conference, Barcelona, Spain, 2005.
- [35] P. Vogel, Application of Wave Field Synthesis in Room Acoustics, Ph.D. thesis, Delft University of Technology, Delft, Netherlands, 1993.
- [36] F. Jacobsen, Report No. 27, the Diffuse Sound Field, Statistical Considerations Concerning the Reverberant Field in the Steady State, The Acoustics Laboratory, Technical University of Denmark, Lyngby, Denmark, 1979, p. 136.
- [37] F. Fahy, P. Gardonio, Sound and Structural Vibration, Radiation, Transmission and Response, Second Edition, Academic Press, The Netherlands, 2007.
- [38] J.W. Rouse, M. Mesh, E.C. Stasiunas, Analytical modeling of the acoustic field during a direct field acoustic test, *J. IEST* 54 (2011) 1–54.